May 2014
Volume 120
Issue 1937
£5.10

www.electronicsworld.co.uk

Electronics WORLD

THE ESSENTIAL ELECTRONICS ENGINEERING MAGAZINE

EMI Reduction In Industrial Environments

A new solution

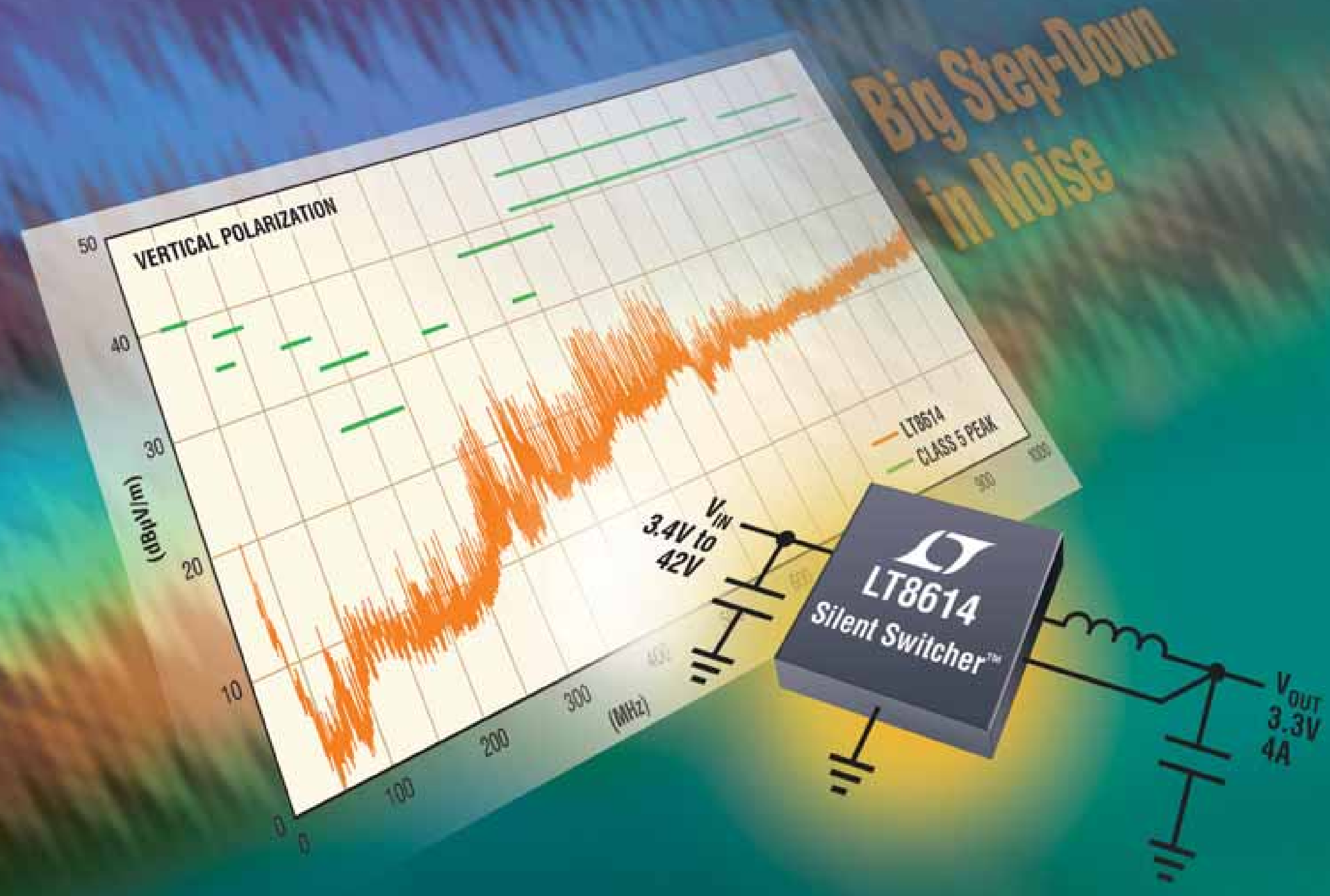

News
3D printing reaches new heights

RF and Microwave
Reformulating mathematics for easier point-source radiation calculations

Special Report: Aerospace
Autonomous navigation for a quadrotor aircraft

Cover supplied by
LINEAR TECHNOLOGY
More on pages 8-9

REGULARS

FEATURES

DEUTSCHE TELEKOM'S M2M PREDICTIONS FOR 2014

> "The targeted point of arrival is the Smart Factory which is ruled by completely new modes of production

Machine-to-machine communication (M2M) and the Internet of Things (IoT) run through all areas of life and work. Cars, cargo containers, parking spaces or even wristwatches and coffee cups – everything around us is on the verge of being connected. To shape this development and make its benefits available to both businesses and private individuals, various companies are actively engaging in the M2M ecosystem and have been for several years. Currently, there are over 600 companies from 56 countries participating in the M2M Partner Program, a global platform for offering and finding M2M solutions. Deutsche Telekom is also offering the M2M Marketplace, the world's first online shop dedicated to M2M and IoT, established in 2012. Developers can find there everything needed to connect machines and create new solutions.

For 2014, Deutsche Telekom expects the following developments:

- Smart Factories to foster individual manufacturing: Industrial applications are the all-time high of M2M. Initiatives such as Industry 4.0 (German government initiated high-tech strategy) bring connected technologies in manufacturing processes back into the spotlight. The targeted point of arrival is the Smart Factory, governed by completely new modes of production. It takes individual customer requirements into consideration, and models both business and engineering processes dynamically. The Smart Factory can adapt quickly to changing demands, and handles resources more efficiently than before.
- M2M in the automotive industry – the aftermarket is up and coming: The automotive industry continues to be one of the biggest growth areas. Applications such as predictive maintenance, entertainment services and remote monitoring, including more comprehensive fleet management solutions, drive the market for connected cars. Since automobile manufacturers will need a few years to implement the technology, there is a huge opportunity for the automotive aftermarket. In 2014, more M2M solutions for car dealers will enter the market which will offer value-added services to their customers, independent of car manufacturers.
- Big Data Analytics: Combining different data sources will generate new services. Since Big Data Analytics entered the M2M stage, several evaluation solutions for different segments have emerged. Today, we can analyze massive amounts of data generated by wind turbines, for example, to predict potential faults and make sure everything works as efficiently as possible. But this is just the beginning. The next phase of Big Data Analytics will bridge the gaps between different domains and generate new services, by combining machine data with information from the Internet, such as weather reports or posts from social media and collaboration platforms.
- Breaking new ground – M2M targets consumer markets: Today, most companies engaged in M2M are driven by B2B transactions. In the years to come, more of them will engage in the IoT and consumer-related products. We expect personal tracking devices and wearable technology to boom this year. Examples include data glasses and smart watches, as well as health and fitness devices that monitor vital signs such as respiration and body temperature or heart rate. Decreasing prices of track-and-trace modules suggest that we will also witness the next generation of small and affordable tracking solutions entering the market.
- Smart Cities drive M2M in the public sector: M2M is an enabling technology for Smart City applications such as parking management and remote control of street lights. Rising populations and declining budgets will drive cities to deploy connected ICT solutions. These solutions make complex administrative tasks manageable, build sustainable and competitive structures and, ultimately, improve the level of service for citizens. In 2014, lighthouse projects for smarter cities are likely to appear, which give us a foretaste of what is to come in the next few decades.
- Global alliances will expand: Since M2M is a global business and even SMEs are continuously going in for global operations, alliances will be more important than ever. They are key to providing seamless M2M services in all countries and are necessary to improving quality of service and establishing M2M communication standards. In November 2013, the Global M2M Association expanded into Asia and North America and this year these efforts and initiatives will further expand and even consolidate.

Deutsche Telekom is an active participant and enabler of machine-to-machine communication (M2M) and the Internet of Things (IoT). To find out more go to m2m.telekom.com

EDITOR: Svetlana Josifovska
Tel: +44 (0)1732 883392
Email: svetlanaj@sjpbusinessmedia.com

SALES: John Steward
Tel: +44 (0)20 7933 8974
Email: johns@sjpbusinessmedia.com

DESIGN: Tania King
PUBLISHER: Wayne Darroch

ISSN: 1365-4675

PRINTER: Buxton Press Ltd

SUBSCRIPTIONS:
Subscription rates:
1 year: £59 (UK);
£85 (worldwide)
Tel/Fax +44 (0)1635 879361/868594
Email: electronicsworld@circdata.com

SJP business media

Follow us on Twitter @electrowo

Join us on LinkedIn

RESEARCHERS DEVISE NEW, STRETCHABLE ANTENNA FOR WEARABLE HEALTH MONITORING

Researchers from the North Carolina State University have developed a new, stretchable antenna that can be incorporated into wearable technologies, such as health monitoring devices.

"Many researchers – including our lab – have developed prototype sensors for wearable health systems, but there was a clear need to develop antennas that can be easily incorporated into those systems to transmit data from the sensors, so that patients can be monitored or diagnosed," says Dr Yong Zhu, an associate professor of mechanical and aerospace engineering at NC State and senior author of a paper describing the work.

The extremely flexible antennas contain silver nanowires and can be incorporated into wearable health monitoring devices
[Photo: Amanda Myers]

The goal was to develop an antenna that could be stretched, rolled or twisted and always return to its original shape, because wearable systems can be subject to a variety of stresses as patients move around and come into contact with the environment.

To create an appropriately resilient, effective antenna, the researchers used a stencil to apply silver nanowires in a specific pattern and then poured a liquid polymer over the nanowires. When the polymer sets, it forms an elastic composite material that has the nanowires embedded in the desired pattern.

This patterned material forms the radiating element of a microstrip patch antenna. By manipulating the shape and dimensions of the radiating element, the researchers can control the frequency at which the antenna sends and receives signals. The radiating layer is then bonded to a "ground" layer, which is made of the same composite, except it has a continuous layer of embedded silver nanowires.

The researchers also learned that, while the antenna's frequency does change as it is stretched (since that changes its dimensions), the frequency stays within a defined bandwidth.

"This means it will still communicate effectively with remote equipment while being stretched," said Zhu. "In addition, it returns to its original shape and continues to work even after it has been significantly deformed, bent, twisted or rolled." As the frequency changes almost linearly with the strain, the antenna can be used as a wireless strain sensor as well.

"Other researchers have developed stretchable sensors, using liquid metal, for example," said Zhu. "Our technique is relatively simple, can be integrated directly into the sensors themselves and would be fairly easy to scale up."

The work on the new, stretchable antenna builds on previous research at Zhu's lab to create elastic conductors and multifunctional sensors using silver nanowires.

3D PRINTING TRIALS OF UNMANNED AIRCRAFT IN SHEFFIELD

Engineers at the Advanced Manufacturing Research Centre (AMRC) at the University of Sheffield have successfully printed a 1.5m-wide prototype unmanned aerial vehicle (UAV) for a research project looking at 3D printing of complex designs.

The engineers said the polymer craft could form the basis of cheap and potentially disposable UAVs that could be built and deployed in remote situations potentially within as little as 24 hours.

Earlier versions required significant amounts of support material around component parts to prevent the airframe structures from deforming during the build process. Using support material adds a direct material cost and significantly increases build time, in some cases by an order of magnitude. This is a result of the machine having to change between build and support structure heads after each printed layer.

New 3D printing techniques, such as the fused deposition modelling (FDM) used to make the UAV at Sheffield University, could soon be used in the creation of products without the need for complex and expensive tooling and the time required in traditional manufacturing.

The UAV has already completed a test flight as a glider. Researchers are developing an electric ducted fan propulsion system that will be incorporated into the airframe's central spine. They plan to develop the craft for guidance by GPS or camera technology, controlled by an operator wearing first-person-view goggles.

"Following successful flight testing, we are working to incorporate blended winglets and twin ducted fan propulsion. We are also investigating full on-board data logging of flight parameters, autonomous operation by GPS, and control by surface morphing technology. Concepts for novel ducted fan designs are also being investigated," said Dr Garth Nicholson, who led the project.

The Sheffield University UAV has nine parts that snap together. It weighs less than 2kg and is made from thermoplastic.

The engineers are currently evaluating the potential of nylon as a printing material that would make the UAV 60% stronger with no increase in weight.

The 3D printed UAV in flight (top) and in the lab (bottom)


WHO'S BEST TO
DEPEND
ON FOR THE PARTS I NEED?
DO THEY STOCK A
WIDE RANGE
OF PARTS FROM
LEADING BRANDS?
NO
Don't settle for second best.
YES
We can offer around 500,000 parts from over 2,500 brands you know and trust.
IF I ORDER TODAY CAN THEY
DELIVER
TOMORROW?
NO
Don't risk it.
YES
We offer same-day despatch with free next working day delivery (conditions apply) on purchases above £20 (excl. VAT).
IS IT
EASY
TO FIND THE PARTS I NEED?
NO
Aaargh!
YES
Our website makes it simple and efficient to find what you need.
DO THEY HAVE GREAT
CUSTOMER
SUPPORT?
NO
Uh oh...not good.
YES
Our fast, friendly help and support team is only a call away.
DO THEY OFFER
VALUE FOR
MONEY?
NO
YES
Our one-stop, hassle-free approach saves you time and money, while regular price checks and large order discounts keep us competitive.
You can count on us for the parts you need
Beyond delivering on time, every time for over 75 years, RS Components delivers something you can't put a price on. Peace of mind.
rswww.com
RS

EMI REDUCTION IN INDUSTRIAL ENVIRONMENTS

by Tony Armstrong, Director of Product Marketing, Power Products & Christian Kück, Strategic Marketing Manager, Power Management Products, Linear Technology Corporation

Background

Component selection and circuit board layout play a significant role in determining the success or failure of virtually all power supplies. These aspects set their functional, electromagnetic interference (EMI) and thermal behaviour. For the un-initiated, switching power supply layout may seem like a "black" art, but it is in-fact a basic aspect of a design which is often overlooked in the early stages of the process. Since functional EMI requirements always have to be met, what is good for functional stability of the power supply is also usually good for its EMI emissions too. Furthermore, good layout from the beginning does not add any cost to the design, but it can actually provide cost savings by eliminating the need for EMI filters, mechanical shielding, EMI test time and numerous board revisions.

Moreover, the potential problem for interference and noise can be exasperated when multiple DC/DC switchmode regulators are paralleled for current sharing and higher output power. If all are operating (switching) at a similar frequency, the combined energy generated by multiple regulators in a circuit is then concentrated at one frequency. Presence of this energy can become a concern especially if the rest of ICs on the printed circuit boards (PCBs), as well as other system boards are close to each other and susceptible to this radiated energy. This can be particularly troubling in industrial automation systems which are densely populated and are often in close proximity to electric noise generating sources, such as mechanically switched inductive loads, PWM drive power outputs, microprocessor clocks and contact switching.

Addressing Switching Regulator Noise Emissions

In an industrial environment, switching regulators usually replace linear regulators in areas where low heat dissipation and efficiency are valued. Moreover, the switching regulator is typically the first active component on the input power bus line, and therefore has a significant impact on the EMI performance of the complete converter circuit.

There are two types of EMI emissions; conducted and radiated. Conducted emissions ride on the wires and traces that connect up to a product. Since the noise is localised to a specific terminal or connector in the design, compliance with conducted emissions requirements can often be assured relatively early in the development process with a good layout or filter design as already stated.

Radiated emissions, however, are another story. Everything on the board that carries current radiates an electromagnetic field. Every trace on the board is an antenna and every copper plane is a resonator. Anything, other than a pure sine wave or DC voltage, generates noise all over the signal spectrum. Even with careful design, a power supply designer never really knows how bad the radiated emissions are going to be until the system gets tested. And radiated emissions testing cannot be formally performed until the design is essentially complete.

Filters are often used to reduce EMI by attenuating the strength at a certain frequency or over a range of frequencies. A portion of this energy that travels through space (radiated) is attenuated by adding metallic and magnetic shields. The part that rides on PCB traces (conducted) is tamed by adding ferrite beads and other filters. EMI cannot be eliminated but can be attenuated to a level that is acceptable by other communication and digital components. Moreover, several regulatory bodies enforce standards to ensure compliance.

Modern input filter components in surface mount technology have better performance than through-hole parts. However, this improvement is outpaced by the increase in operating switching frequencies of switching regulators. Higher efficiency, low minimum on- and off-times result in higher harmonic content due to the faster switch transitions. For every doubling in switching frequency, the EMI becomes 6dB worse while all other parameters, such as switch capacity and transition times, remain constant. The wideband EMI behaves like a first order high pass with 20dB higher emissions if the switching frequency increases by 10 times.

Savvy PCB designers will make the hot loops small and use shielding ground layers as close to the active layer as possible. Nevertheless, device pin-outs, package construction, thermal design requirements and package sizes needed for adequate energy storage in decoupling components dictate a minimum hot loop size. To further complicate matters, in typical planar printed circuit boards, the magnetic or transformer style coupling between traces above 30MHz will diminish all filter efforts since the higher the harmonic frequencies are the more effective unwanted magnetic coupling becomes.

A New Solution to these EMI issues

The tried and true solution to EMI issues is to use a shielding box for the complete circuit. Of course, this adds costs, increases required board space, makes thermal management and testing more difficult, as well as introducing additional assembly costs. Another frequently used method is to slow down the switching edges. This has the undesired effect of reducing the efficiency, increasing minimum on-, off-times, and their associated dead times and compromises the potential current control loop speed.

Linear's recently introduced LT8614 Silent Switcher™ regulator, delivers the desired effects of a shielded box without using one, and so eliminates the above mentioned drawbacks. See Figure 1. The LT8614 also has a world class low I_Q of only 2.5µA operating current. This is the total supply current consumed by the device, in regulation with no load.

Its ultralow dropout is only limited by the internal top switch. Unlike alternative solutions, the LT8614's R_{DSON} is not limited by maximum duty cycle and minimum off-times. The device skips its switch-off cycles in dropout and performs only the minimum required off cycles to keep the internal top switch boost stage voltage sustained.

At the same time, the minimum operating input voltage is only 2.9V typical (3.4V maximum), enabling it to supply a 3.3V rail with the part in dropout. The LT8614 has higher efficiency than the LT8610/11 at high currents since its total switch resistance is lower. It can also be synchronised to an external frequency operating from 200KHz to 3MHz.

The AC switch losses are low, so it can be operated at high switching frequencies with minimal efficiency loss. In EMI-sensitive applications, such as those commonly found in many industrial environments, a good balance can be attained and the LT8614 can run either at low hundreds of KHz or above 2MHz. In a setup with 700KHz operating switching frequency, the standard LT8614 demo board does not exceed the noise floor in a CISPR25 measurement.

The Figure 2 measurements were taken in an anechoic chamber under the following conditions: 12V in, 3.3V out at 2A with a fixed switching frequency of 700kHz.

To compare the LT8614 Silent Switcher technology against another current state-of-the-art switching regulator, the part was measured against the LT8610. The test was performed in a GTEM cell using the same load, input voltage and the same inductor on the standard demo boards for both parts.

One can see that up to a 20dB improvement is attained using the LT8614 Silent Switcher technology compared to the already very good EMI performance of the LT8610, especially in the more difficult to manage high frequency area. This enables simpler and more compact designs where the LT8614 switching power supply needs less filtering compared to other sensitive systems in the overall design.

In the time domain, the LT8614 shows very benign behaviour on the switch node edges, as shown in Figure 4. Even at 4ns/div this Silent Switcher regulator shows very low ringing (see Ch2 in Figure 3). The LT8610 has a good damped ringing (Ch1, Figure 3) but one can see the higher energy stored in the hot loop compared to the LT8614 (in Ch2).

All time domain measurements in Figures 3 and 4 were done with 500MHz Tektronix P6139A probes with close probe tip shield connection to the PCB GND plane, both on the standard demo boards.

The LT8614's low minimum on-time of 30ns enables large step-down ratios even at high switching frequencies. As a result, it can supply logic core voltages with a single step-down from inputs up to 42V.

Conclusion

It is well known that EMI considerations for industrial environments require careful attention during the initial design process in order to ensure that they will pass EMI testing once the system is completed. Until now, there was not a sure way to guarantee that this could easily be attained with the right power IC selection. This has now changed due to the introduction of the LT8614 Silent Switcher regulator. This new device reduces EMI from current state-of-the-art switching regulators by more than 20dB, while increasing conversion efficiencies with no drawbacks. A 10 fold improvement of EMI in the frequency range above 30MHz is attained without compromising minimum on- and off-times or efficiency in the same board area. This is accomplished with no special components or shielding, representing a significant breakthrough in switching regulator design. This is just the sort of breakthrough product that allows industrial automation system designers take their products to the next level of noise performance.

Linear Technology (UK) Ltd
Tel: 01628 477066
Email: uksales@linear.com • www.linear.com

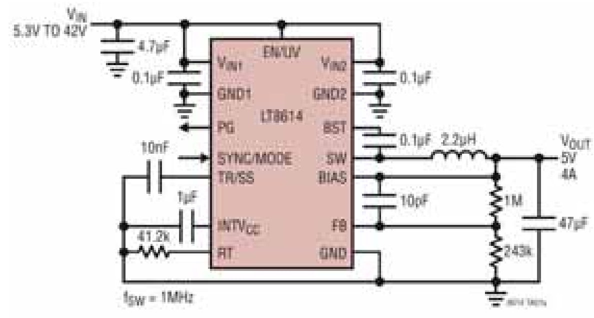

Figure 1: The LT8614 Silent Switcher minimises EMI/EMC emissions while delivering high efficiency at frequencies up to 3MHz.

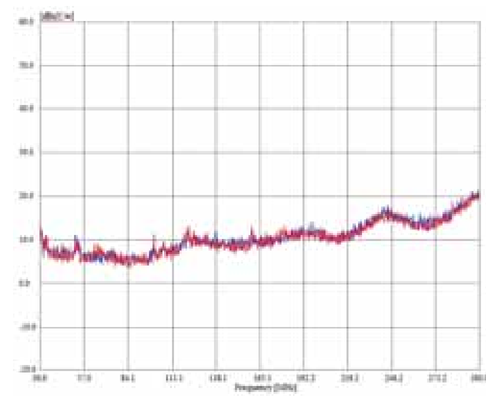

Figure 2: Blue trace is the noise floor; red trace is the LT8614 board at CISPR25 radiated measurement in an anechoic chamber.

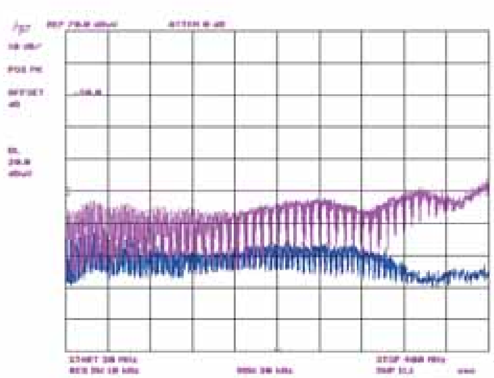

Figure 3: Blue trace is the LT8614, purple trace is the LT8610; both $13.5V_{IN}$, $3.3V_{OUT}$ at 2.2A load.

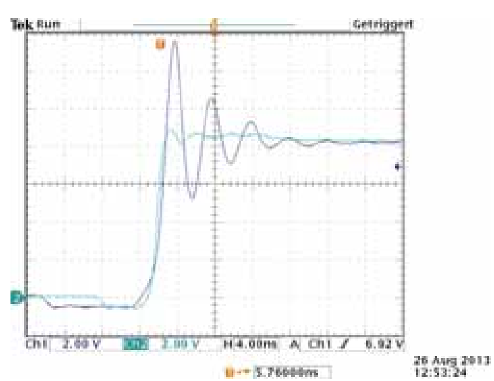

Figure 4: Ch1: LT8610, Ch2: LT8614 switch node rising edge both at $8.4V_{IN}$, $3.3V_{OUT}$ at 2.2A.

Narrowband Radios, VHF ISM Bands and 169MHz

MYK DORMER IS A SENIOR RF DESIGN ENGINEER AT RADIOMETRIX LTD **WWW.RADIOMETRIX.COM**

Low-power radio devices surround us in every walk of life, from the Bluetooth connectivity built into mobile phones to the wireless key-fobs that lock and unlock cars. Beyond that, there are untold numbers of industrial and commercial radio links, in thousands of diverse, unseen applications.

These devices all owe their popularity to the existence of designated license-free Short-Ranged Device (SRD) band allocations which permit a specification-compliant (and tested) radio link to be operated without further regulatory interference, such as user training, or the necessity to purchase specific operating licenses.

In recent years the technical press and engineering community at large have concentrated on ever more sophisticated wireless network devices, to the point that it seems on first inspection that all short-ranged wireless applications can be fulfilled by a 2.45GHz band wireless network device, either ZigBee or Bluetooth or one of their imitators.

The truth of the matter is – as usual! – far more complex. These proprietary architecture short-range radio devices do offer some very desirable capabilities. The mesh-network architectures can provide robust connections, while the high data-transfer rates allow almost Internet-like functions to be supported, and the interfaces provide a programmer-friendly, software-heavy environment, with abundant support tools. But they are far from the only short-range radio solutions in use.

The term 'SRD' still refers to a wide class of data communication radios with RF power outputs from below a milliwatt, to over half a watt, operating at ranges up to 1km (...although specialized, low data-rate VHF units can exceed 10km). Data rates vary from below 100bit/s, to over 1Mbit/s.

To properly understand the merits and problems of these different wireless systems, it is necessary to examine a little basic radio theory:

Transmitter Power

For the purposes of SRD applications this is limited by the relevant regulations and by available power supplies (frequently batteries, with limited capacity and peak current ratings).

10mW is probably the most common transmit power, but up to 500mW (+27dBm) is usable on some subbands, and this stands as the informal maximum for "low power" radio systems.

Channel Bandwidth

This defines maximum data throughput but also, inversely, receiver sensitivity. SRD radios generally are either wideband (high data-rate, short range) or narrowband (lower data speeds, long range).

Operating Frequency

Although this is limited by permitted band allocations in the region where the radio is to be used, the choice of operating frequency has perhaps the greatest absolute effect on the nature of the communication link.

It carries many implications: lower frequency circuitry can draw less current and be easier to design, but is often bigger, as single-chip implementations are often unavailable for bands much below 150MHz.

At higher frequencies the aerials are more compact for a given level of performance. And, most importantly, path loss, (and thus range for a given transmitter power and receiver sensitivity) relates directly to the operating frequency. To relate these to practical SRD data radios:

Narrowband units use channel spacing of 25kHz or less and data rates below 10kbit/s. Wideband radios typically have channel spacing of 200kHz or more

	2.45GHz band	VHF (for example, 169MHz)
Range	Limited (10-100m)	Long (over 1km)
Building penetration	Poor (line of sight)	Good
Aerial	Small	Large (or complex)
Interface	Complex	Simple
	Mesh network	Star (point to [multi] point)
Data rate	High (> 250kbit/s)	Low (less than 10kbit/s)
Protocols	Open (ZigBee, etc)	User defined
Average power	Low	Low
Peak current	Moderate - high	Low
Cost	Low	Moderate

Table 1: Wireless band comparisons

and data rates exceeding 64kbit/s (typical 2.45GHz band units have proportionately even wider channels: IEEE802.15.4-based radios use 5MHz channel spacing, at 250kbit/s).

Beyond the available-spectrum usage implications, the less obvious trade-off here is in sensitivity and hence range for a given transmitter power.

Each doubling of the signal bandwidth unavoidably degrades receiver signal-to-noise (S/N) ratio, and hence sensitivity, by 3dB. So, while a narrowband 12.5kHz unit might have a sensitivity of -118dBm (at 2.5kbit/s), a comparable wideband unit might achieve only -107dBm at 64kbit/s (and will require a 600kHz wide channel). For the same transmitter power this will result in less than half the range, compared to the narrowband radio.

Path loss is related to frequency – no matter which propagation model is used – it is proportional to 20log(f). This means, assuming aerial performance and receiver sensitivity were identical:

10mW at 169MHz
80mW at 433MHz
250mW at 869MHz
2W at 2.45GHz would have the same range.

In practice, this effect is even more pronounced, as the higher frequency radios tend to be high data-rate designs, with consequently lower receive sensitivity, while VHF units are invariably the more sensitive narrowband types. Typical sensitivity figures are -120dBm for a 169MHz unit, compared to -104dBm for a good ZigBee node, inferring a total link budget advantage of 40dB or, in simpler terms, ten times the range, for the same transmitter power.

At this point it is possible to draw certain conclusions:

- Only at higher frequencies is there sufficient raw spectrum allocated to support high data rates. Systems streaming large blocks of data (digital video, high-quality digital audio, wireless LANs) and designs with large amounts of overhead in their interface design (Internet protocols, complex network structures) will always be best suited to the 2.4GHz band and, to a lesser extent, the 869MHz band.
- A higher data-rate will always incur a sensitivity (and hence range) penalty, compared to a slower link (assuming all other factors are equal), and a lower frequency link will always exhibit a lower path loss (and hence longer range), until the point at which its aerial performance is compromised by physical size restrictions. A 10mW 2.4GHz mesh radio will always be significantly out-ranged by a VHF narrowband design of similar power.

If data rate and cost are crucial factors, if a complex protocol interface is needed, or if multiple users are accommodated by duty cycle or time division duplexing, then choose a wideband module on the 2.4GHz band. But if range, resistance to interferers, better power efficiency, or multiple channel operation are required, then a narrowband radio module is the better choice. There are a lot of options below 1GHz. ●

INVESTIGATION OF A PLANAR ANTENNA WITH BANDWIDTH ENHANCEMENT FOR X-BAND APPLICATIONS

M. R. I. FARUQUE, M. M. ISLAM AND **M. T. ISLAM**, FROM THE UNIVERSITI KEBANGSAAN MALAYSIA, PRESENT A PLANAR ANTENNA DESIGN FOR X-BAND APPLICATIONS

Planar antennas play an important role in wireless communications systems and they continue to face shifting demands for a new generation of antenna technologies.

One of the widely used antennas is the microstrip patch, as it offers a low profile, conformal design, ease of manufacture and integration, and it is low cost and lightweight. Its main disadvantages, however, are narrow bandwidth and low efficiency, so increasing its bandwidth is the main focus of many research projects.

Communications in the X-Band

X-band (8GHz-12GHz) technology has been broadly used in various applications because of the high data-transmission rate, large bandwidth and short-range features. An electronically reconfigurable unit cell has been discussed with two phase states in X-band applications for linear polarization of the transmitting arrays in Reference 1. A wide-slot microstrip antenna has been designed [2] using a fork-like tuning stub to increase the bandwidth, achieving 1.1GHz with a gain of below 1.5dBi over the complete operational frequency band.

A wide-band rectangular patch antenna with a single layer

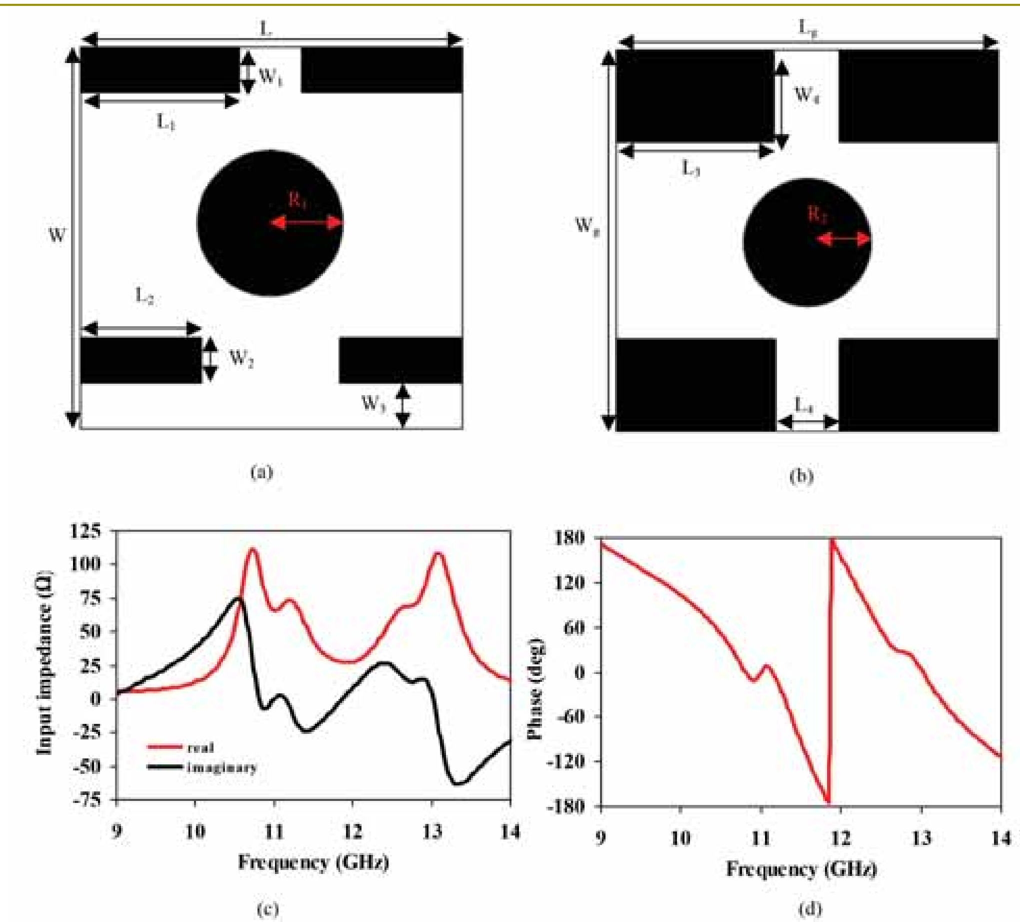

Figure 1: The proposed X-band planar antenna: (a) Front view; (b) Back view; (c) Input impedance; (d) Phase value

was proposed in Reference 3, where impedance bandwidth of more than 20% was achieved. A rotated slotted antenna was proposed for enhancing the bandwidth, printed on FR4 substrate material [4]. This antenna had a bandwidth of about 2.2GHz, as well as a gain change of below 2dBi. However, this antenna's dimensions are $70\times70mm^2$, which is too large.

A CPW (coplanar waveguide) fed loop slot antenna with a tuning stub was used to amplify the bandwidth. Its area and gain range of 3.75-4.88dBi over the desired operational frequency band, with a suitable position of the widened tuning stub, allowed a good bandwidth to be achieved [5]. By using such bandwidth enhancement techniques, the CPW-fed slotted antennas showed 34% to 60% impedance bandwidth.

Then, two E-shaped slot antennas were designed by using a microstrip line and CPW as the feed transmission line for broadband applications [6]. The antenna's size was $85\times85mm^2$ with a reasonable radiation pattern and improved bandwidth. However, its weak point is its large size.

A novel design of a gap-coupled sectoral patch antenna for X-band applications was presented in Reference 7. This research investigated the bandwidth enhancements for a planar X-band antenna, and the effect on the antenna parameters and desired resonances with circular and rectangular slots on the ground plane and a radiating patch.

Work on the design of this type antennas continues, and various techniques are being used, including increased substrate thickness, changing the patch by cutting rectangular slots and the ground plane. The goal is to achieve the desired parameters such as good impedance matching, gain, radiation pattern, return loss, efficiency and Smith chart performance.

Antenna Design Specifications

Figure 1 shows the geometry of our proposed X-band planar antenna. The antenna comprises circular and rectangular slots on both, the radiating patch and ground plane. It is printed on a 1.6mm-thick FR4 substrate with a dielectric loss tangent of 0.02, relative permittivity of 4.60 and relative permeability of 1.

A microstrip line is used as feed line, with a 50Ω SMA connector for the input. Figure 1c shows the input impedance with real and imaginary values. Figure 1d shows the linear phase variations plotted against frequency.

The geometry of the proposed microstrip antenna was designed using equations from the transmission line model (TEM) approximation, in which the radiating patch is shown as a transmission line resonator with no transverse field variations. The length and width of the microstrip patch antenna can be modelled in accordance with the resonant frequency using Equations 1-4.

$$W=\frac{c}{2f_o}\sqrt{\frac{\varepsilon_r+1}{2}} \qquad (1)$$

$$L=\frac{c}{2f_o\sqrt{\varepsilon_r}}-2\Delta l \qquad (2)$$

where W is the width of the radiating patch, L is its length, *f0* is the desired resonance and *c* is the light speed in a vacuum. The effective dielectric constant is determined using the following equation:

$$\varepsilon_e=\frac{1}{2}(\varepsilon_r+1)+\frac{1}{2}(\varepsilon_r-1)\sqrt{(1+\frac{10h}{W})} \qquad (3)$$

where ε_r is the substrate dielectric constant and the thickness of the substrate is *h*. Electrically, there's a fringing field around the edges if the patch, and *Δl* takes into account this effect, which can be explained as:

$$\Delta l=0.412h\frac{(\varepsilon_e+0.3)[\frac{w}{h}+0.8]}{(\varepsilon_e-0.258)[\frac{w}{h}+0.8]} \qquad (4)$$

The required dimensions have been ascertained as: L = 40mm, W = 40mm, L_g = 40mm, W_g = 40mm, R_1 = 7.5mm, R_2 = 6.5mm, L_1 = 17mm, L_2 = 12mm, L_3 = 17mm, L_4 = 6mm, W_1 = 4mm, W_2 = 4mm, W_3 = 4mm, and W_4 = 10mm.

Analysis Results

Parametric analysis was used to optimize the antenna parameters. This also helped identify the effects of different parameters of the return losses. Figure 2a shows the return losses for different radius R_1 values. It was shown that the achieved bandwidth was low on both lower and upper bands when the radius was 7mm and 8mm; this is why R_1 was optimized at 7.5mm.

Figure 2b shows the return loss for different values of the radius R2, showing that no bandwidth on the upper bands using the value of the radius as 6mm and 7mm. Therefore, the optimized value for the radius R_2 is 6.5mm.

Figure 2c illustrates the return loss for different microstrip-line values, L4. It was found that better bandwidth was attained on both upper and lower bands using 6mm as the microstrip line value. Consequently, the optimized value for R_2 is 6.5mm and L_4 = 6mm.

The simulated return loss of the proposed antenna is shown in Figure 2d. Return losses of -17.14dB and -14.29dB were obtained at two resonant frequencies, 10.25GHz and 11.54GHz respectively. In the operating bands the bandwidth is 1.59GHz, and it also covers the X-band frequencies.

The gain of the proposed antenna is shown in Figure 2e. A 4.31dB gain is obtained in the operating frequency band of 10.25GHz and 11.54GHz respectively. Figure 2f shows the

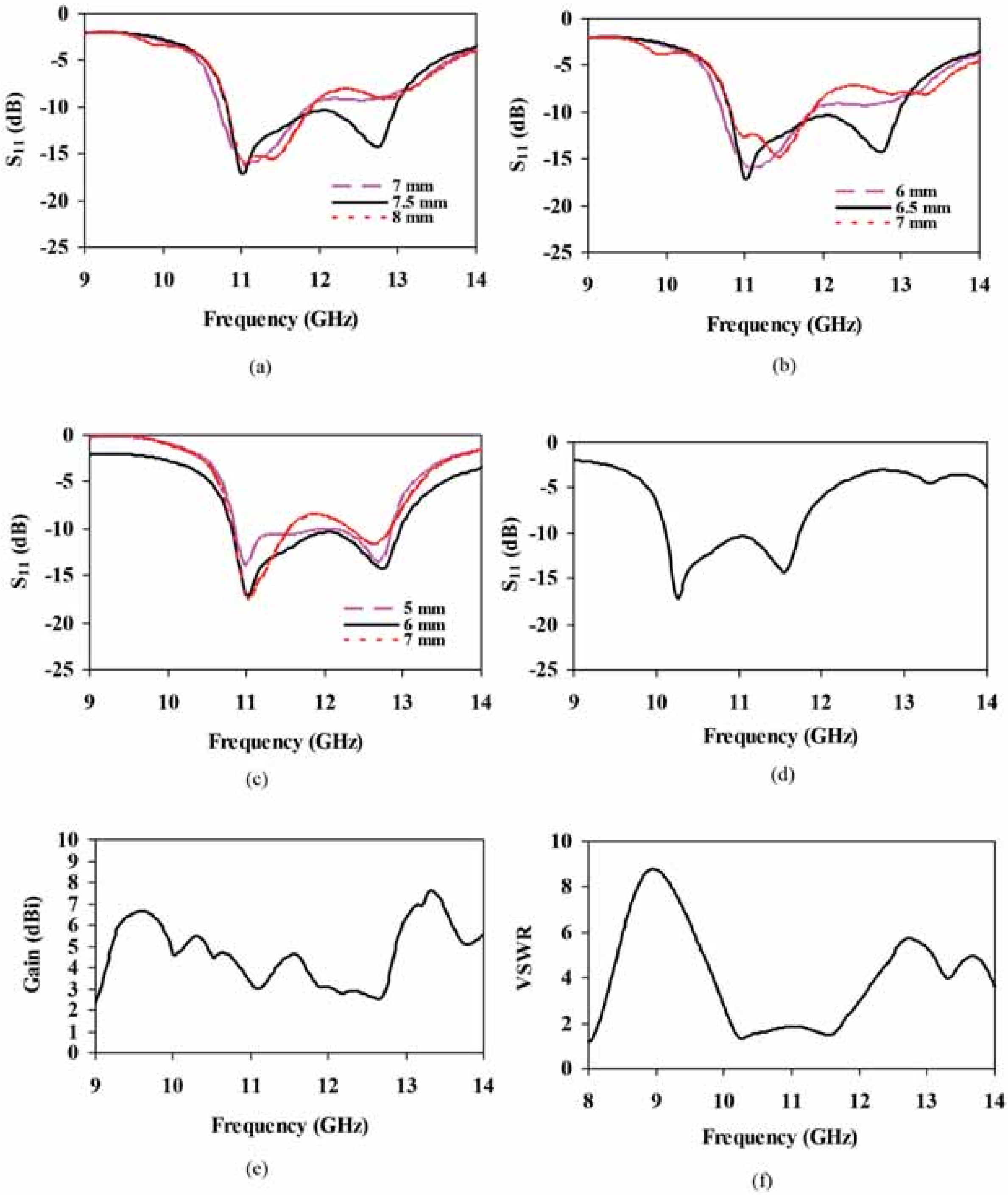

Figure 2: (a) Return losses for different values of radius R1; (b) Return losses for different values of radius R2; (c) Return losses for different values of microstrip line L4; (d) Simulated return losses of the proposed antenna; (e) Simulated gain of the proposed antenna; (f) VSWR of the proposed antenna

voltage standing wave ratio (VSWR) of the proposed antenna. VSWR is below 2, seen in the graph, which is the desired value.

The radiation patterns of the proposed X-band antenna on the E-plane and H-plane at resonant frequencies of 10.25GHz and 11.54GHz are shown in Figure 3. Results show significant omni-directional radiation patterns obtained along the H-plane and E-plane respectively. The E-plane and H-plane co-polarization patterns are omni-directional or nearly omni-directional at a higher frequency. As a result, the radiation pattern of the proposed patch antenna is suitable for X-band applications.

The current distribution of the proposed antenna is shown in Figures 4a and 4b. It can be seen that current flow is maximised when a microstrip line is used as feed line. The current distribution is equal on both the lower and upper radiating elements of the antenna at 8.39GHz. In the 10.25GHz band, current is distributed better than at 11.54GHz and excitation is good in all parts of the antenna except the bottom portion of the transmission line. The Smith chart is plotted in Figure 4c, and Figure 4d shows the radiation efficiency of the antenna to be 78.85%, which is broadly appropriate for X-band applications.

It can be seen that the antenna layout is simple and straightforward, making its fabrication easier. The generalized design procedure for the proposed antenna for dual-frequency operation has also been improved compared to a conventional design. The return losses of -17.14dB and -14.29dB, gain of 4.31dB and bandwidth of 1.59GHz are obtained at two

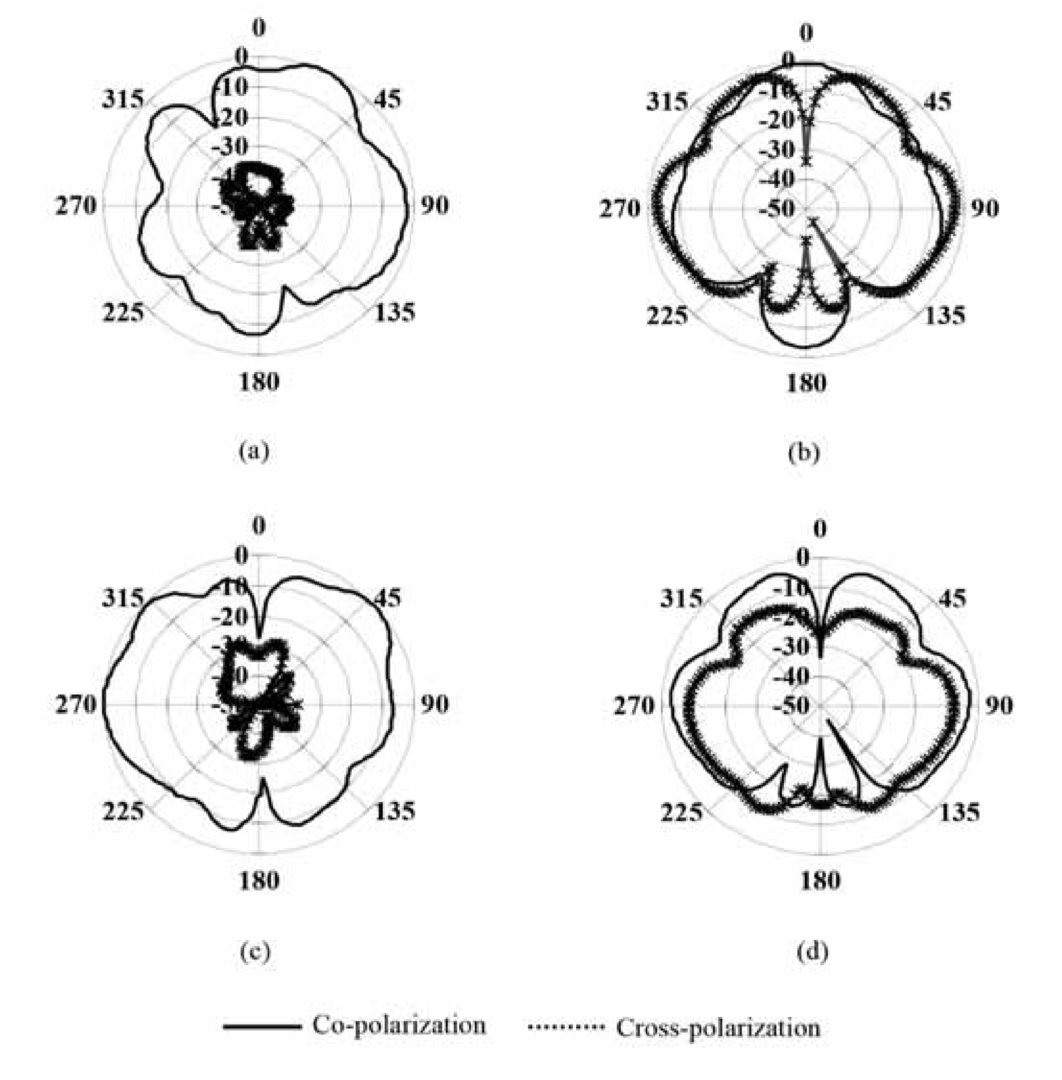

Figure 3: Radiation pattern of the proposed antenna: (a) at 10.25GHz in the E-plane; (b) at 10.25GHz in the H-plane; (c) at 11.54GHz in the E-plane; (d) at 11.54GHz in the H-plane

resonant frequencies, 10.25GHz and 11.54GHz respectively. These simulated results are in agreement. The radiation efficiency of the antenna is 78.85%. These radiation patterns, low cross-polarization, efficiency with improved bandwidth and higher gain make the proposed antenna suitable for use in X-band applications. ●

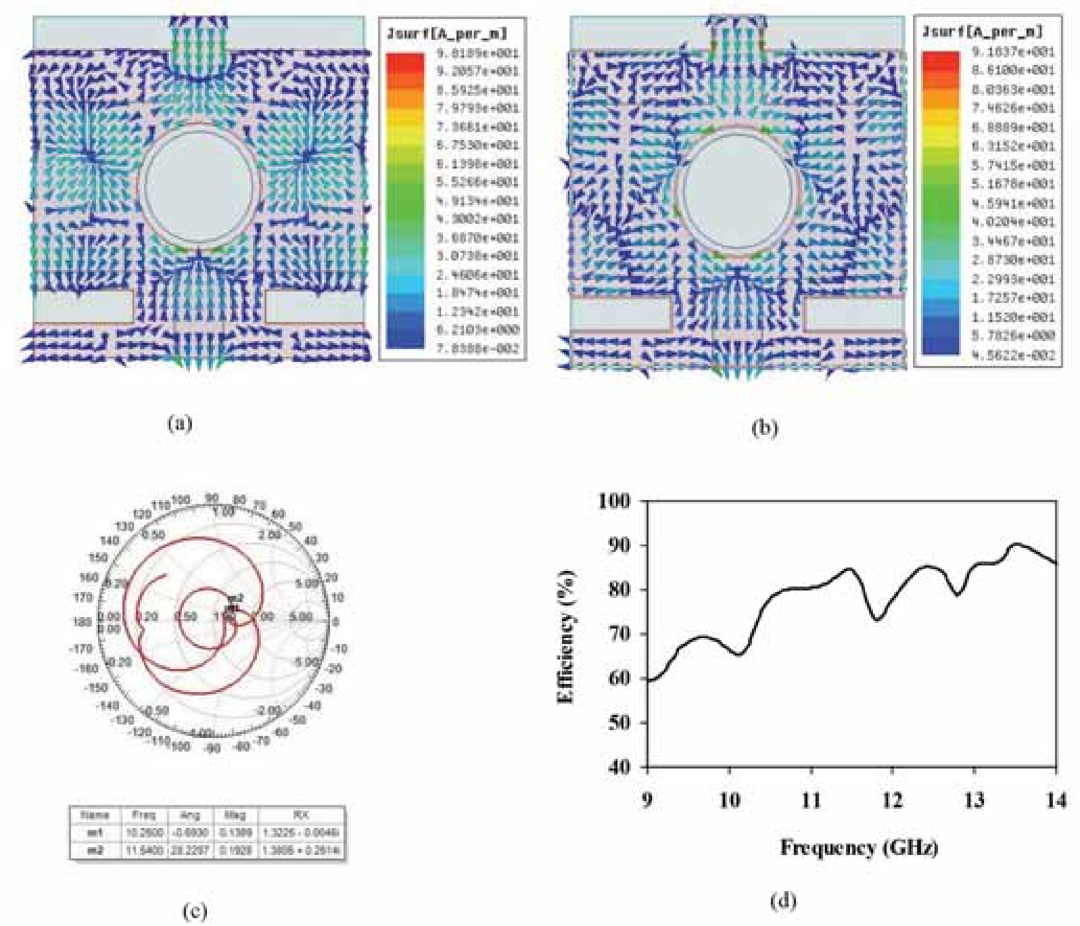

Figure 4: (a) Current distribution at 10.25GHz; (b) Current distribution at 11.54GHz; (c) The Smith chart; (d) Radiation efficiency

REFERENCES

[1] A.Clemente, L. Dussopt, R. Sauleau, P. Potier, P. Pouliguen,"1-Bit Reconfigurable Unit Cell Based on PIN Diodes for Transmit-Array Applications in X-Band," IEEE Transactions on Antennas and Propagation, vol. 60 no. 5, pp. 2260-2269, 2012.

[2] J.-Y. Sze, and K. -L. Wong, "Bandwidth enhancement of a microstrip line-fed printed wide-slot antenna," IEEE Transactions on Antennas and Propagation, vol. 49, no. 7, pp. 1020-1024, 2001.

[3] F. Yang, X. Zhang and Y. Rahmat-samii, "Wide-band E-shaped patch antennas for wireless communications," IEEE Transactions on Antennas and Propagation, vol. 49, no. 7, pp. 1094-1100, 2001.

[4] J.-Y. Jan and J.-W. Su, "Bandwidth enhancement of a printed wide-slot antenna with a rotated slot," IEEE trans. Antennas propag, vol. 53, no.6, pp. 2111-2114, 2005.

[5] H.-D. Chen, "Broadband cpw-fed square slot antennas with a widened tuning stub," IEEE trans. Antennas propag, vol. 51, no. 4, pp.1982-1986, 2003.

[6] A. Dastranj and H. Abiri, "Bandwidth enhancement of printed E-shaped slot antennas fed by CPW and microstrip line," IEEE Transactions on Antennas and Propagation, vol. 58, no. 4, pp. 1402-1407, 2010.

[7] A. Kandwal, S. K. Khah, "A Novel Design of Gap-Coupled Sectoral Patch Antenna," IEEE Antennas and Wireless Propagation Letters vol. 9, pp. 674-677, 2013.


They bring out the best in each other
Honeywell Sensing and Control is a world-class supplier of top quality switches and sensors designed to withstand severe environments.
Aerco is the company's leading MilAero stocking distributor in the UK.
AERCO
HOW CAN I HELP?
Honeywell
aerco.co.uk
sensing.honeywell.com

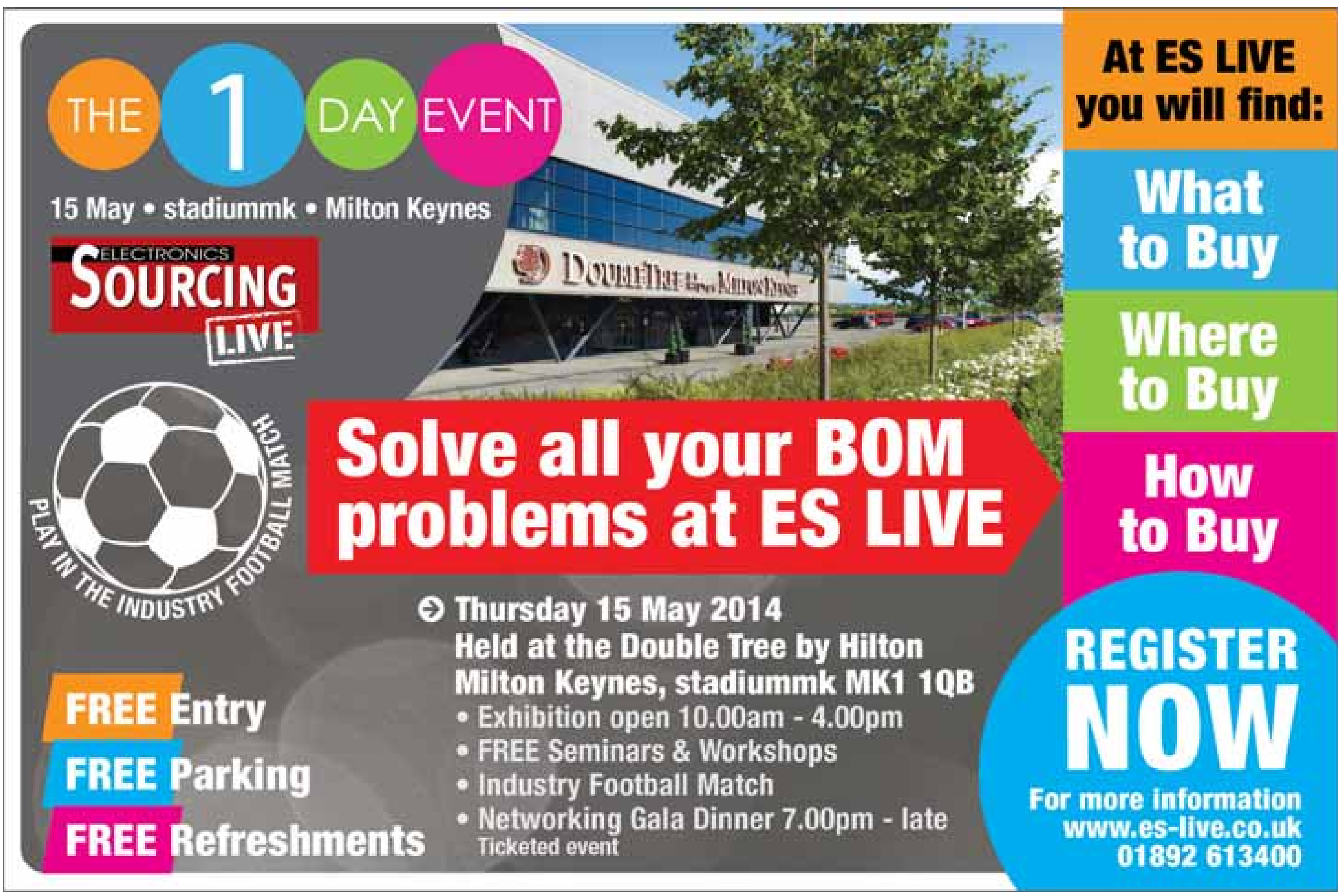
THE 1 DAY EVENT
15 May • stadiummk • Milton Keynes
ELECTRONICS SOURCING LIVE
PLAY IN THE INDUSTRY FOOTBALL MATCH
Solve all your BOM problems at ES LIVE
Thursday 15 May 2014
Held at the Double Tree by Hilton Milton Keynes, stadiummk MK1 1QB
• Exhibition open 10.00am - 4.00pm
• FREE Seminars & Workshops
• Industry Football Match
• Networking Gala Dinner 7.00pm - late
Ticketed event
FREE Entry
FREE Parking
FREE Refreshments
At ES LIVE you will find:
What to Buy
Where to Buy
How to Buy
REGISTER NOW
For more information
www.es-live.co.uk
01892 613400

DUAL DETECTORS WITH DOUBLE-THRESHOLD FOR SPECTRUM SENSING IN COGNITIVE RADIO NETWORKS

ASHISH BAGWARI AND **GEETAM SINGH TOMAR** FROM THE UTTARAKHAND TECHNICAL UNIVERSITY IN INDIA AND THE UNIVERSITY OF THE WEST INDIES, TRINIDAD AND TOBAGO, DESIGN DUAL DETECTORS THAT CONSIST OF A TWO-STAGE SPECTRUM SENSING SCHEME BASED ON COGNITIVE RADIO NETWORKS (CRN)

Cognitive radio (CR) has become a promising technique for solving spectrum scarcity in wireless communications, as wireless services and applications continue to evolve. In CR systems, unlicensed users can use licensed frequencies when the primary user (PU) is not active.

For achieving good spectrum-sensing performance, several methods based on a single CR user have been studied (see Reference [1]). There are three basic spectrum sensing techniques: matched filter detection, energy detection and cyclostationary feature detection [2].

In [3], the authors propose a two-stage spectrum-sensing scheme to improve detection performance. This scheme consists of two detectors: an energy detector (ED) in the first stage and a cyclostationary detector in the second stage. This scheme provides better detection, but is computationally more complex and needs longer sensing time.

Here we present a dual-detector method where the first stage consists of an energy detector with fixed threshold and the second stage is an energy detector (ED) with an adaptive double-threshold (ED_ADT), which optimizes the detection performance at a fixed probability of false alarm (P_f), i.e. 0 or 1, and overcomes any sensing failure problems as well [4].

In the first stage, the ED detects the PU signal. If the received signal energy (X) is greater than a certain threshold (γ), the channel is declared to be occupied; otherwise ED_ADT is performed in the second stage. If the decision metric in this stage exceeds a certain threshold (λ), the channel is declared to be occupied, otherwise it is declared empty and available for a secondary user.

Adaptive double-thresholds such as these are based on upper and lower bounds of the noise uncertainty range [5]. We analyzed the performance of such dual detectors in terms of probability of detection (P_d) and spectrum sensing time (T). Results have shown that the proposed scheme provides better detection performance. The thresholds γ and λ that maximize the probability of detection (with reduced probability of a false alarm) are chosen according to the noise uncertainty at CR user's end.

System Description

CRs use the unused channels of the PU's signal, and a spectrum sensing mechanism allows them to determine the presence of a PU. In this method, the locations of the primary receivers are not known to the CRs, as there is no signalling between the PUs and CRs. To detect the PU signal, we have used the hypothesis for a received signal as described in Reference [6]:

$$x(n) = \begin{cases} w(n), & H_0 \\ s(n)h(n) + w(n), & H_1 \end{cases} \qquad (1)\,(2)$$

In the testing, $x(n)$ shows signals received by each CR user: $s(n)$ is the PU licensed signal, $w(n) \sim N(0, \sigma_w^2)$ is additive white Gaussian noise with zero mean and variance σ_w^2, and $h(n)$ denotes the Rayleigh fading channel gain of the sensing channel between the PU and the CR user. H_0 is the null hypothesis – which indicates that PU is absent; and H_1 is the alternative hypothesis – which indicates that PU is present.

For the detection of unknown deterministic signals corrupted by the additive white Gaussian noise, an ED is derived in [7], called conventional energy detector (CED). This is an easily realized detector of unknown signals in spectrum sensing. It collects the test statistic and compares it to a threshold (γ) to decide whether the PU signal is present or not. The test statistic is given by:

$$X = \frac{1}{N}\sum_{n=1}^{N} |x(n)|^2 \qquad (3)$$

where $x(n)$ is the received input signal, N is the number of samples and X denotes the energy of the received input signal which is compared with the threshold to make the final decision. The threshold value is set to meet the target probability of false alarm P_f according to the noise power. The probability of detection P_d can be also identified. The expressions for P_f and P_d can be followed as [8]:

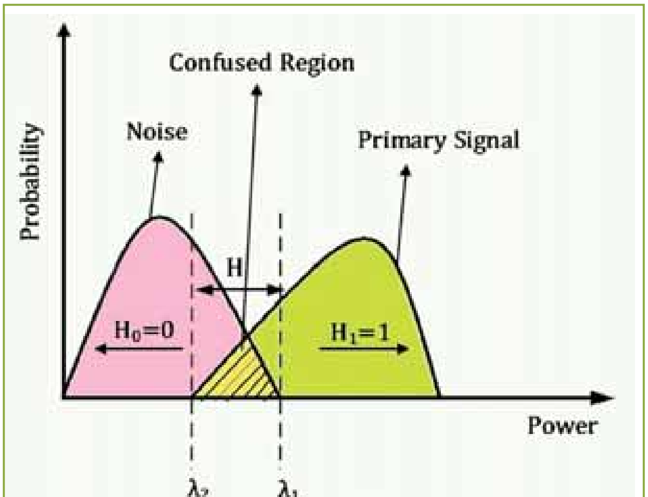

Figure 1: Energy distribution of primary-user signal and noise

$$P_f = P_r(X < \lambda) = Q\left(\frac{\lambda - N\sigma_\omega^2}{\sqrt{2N\sigma_\omega^4}}\right) \quad (4)$$

$$P_d = P_r(X \geq \lambda) = Q\left(\frac{\lambda - N(\sigma_S^2+\sigma_\omega^2)}{\sqrt{2N(\sigma_S^2+\sigma_\omega^2)^2}}\right) \quad (5)$$

where σ_ω^2 and σ_S^2 are the noise variance and signal variance respectively. $Q(\,)$ denotes Gaussian tail probability Q-function. The total error rate is the sum of the probability of false alarm (P_f) and the probability of missed detection alarm (P_m). Hence, the total error probability rate is as follows:

$$P_e = (P_f + P_m) \quad (6)$$
$$P_e = P_f + (1 - P_d) \quad (7)$$

where (1-P_d) shows the probability of missed detection (P_m).

A Double-Threshold Scheme For Spectrum Sensing

In energy detection based spectrum sensing [9], noise uncertainty increases the difficulty in setting the optimal threshold for a CR and thus degrades its sensing reliability [10]. Also this may not be optimum in low SNR conditions where the performance of a fixed single threshold (γ) based detector can vary substantially from the targeted performance metrics.

Figure 1 shows the energy distribution curve between PU and the noise signal. ED with fixed single threshold can easily distinguish PU and noise if they are quite far from each other. But, the problem is, if the signals intersect, then it is very difficult or confusing to identify if the signal is PU or noise; see the region between λ_1 and λ_2 in Figure 1, known as confused region (λ_1 is called upper bound and λ_2 lower bound).
To overcome this problem we introduce an adaptive double-threshold concept, where we use two thresholds λ_1 and λ_2. That they are both adaptive means the selections of these thresholds are purely based on the level of noise variance. The upper bound threshold (λ_1) is chosen as the maximum noise variance, and the lower bound threshold (λ_2) is chosen as the minimum noise variance.

Further, the confused region is divided into four equal levels. If the detected PU signal energy values (X) lie in the confused region, the scheme will generate its respective decimal values, which are then compared with the threshold (λ) to make a local decision at a fixed probability of false alarm (P_f), i.e. 0 or 1. If values exist outside the confused region, the scheme will also generate binary bits, i.e. 0 or 1, depending on the signal's position. Thus numerical results show that the proposed scheme optimizes the detection performance.

The adaptive double-threshold scheme can be described as the following logic rule (LR):

$$LR = \begin{cases} H_0 = 0, X \leq \lambda_2 \\ H = M,\ \lambda_2 < X < \lambda_1 \\ H_1 = 1, \lambda_1 \leq X \end{cases} \quad (8)$$

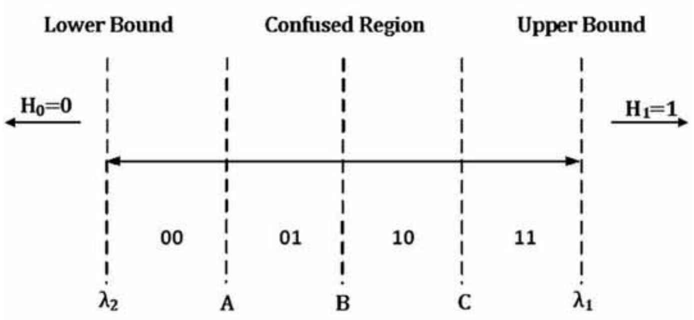

Figure 2: The confused region is divided into four equal quantization intervals using the two-bit quantization method

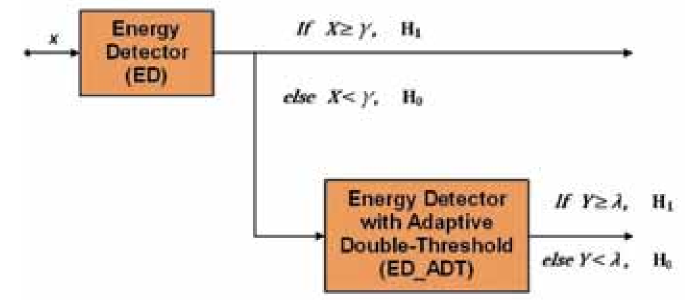

Figure 3: Dual detectors

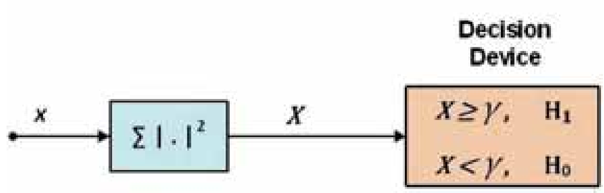

Figure 4: Internal architecture of the first-stage energy detector with single threshold

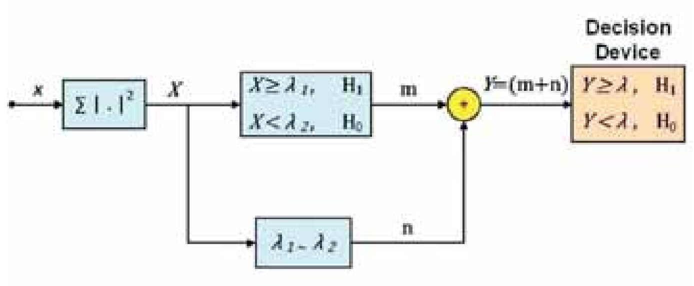

Figure 5: Internal architecture of the second-stage energy detector with adaptive double-threshold (ED_ADT)

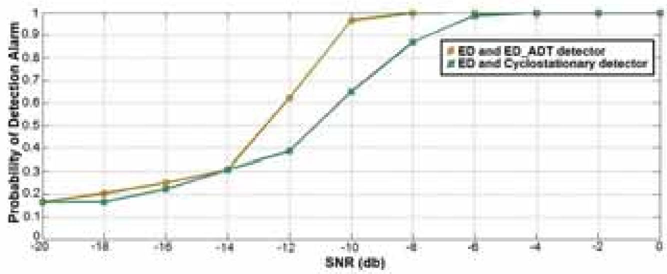

Figure 6: Probability of detection vs SNR at Pf = 0.1 with N = 1000, QPSK modulation scheme and Rayleigh fading channel

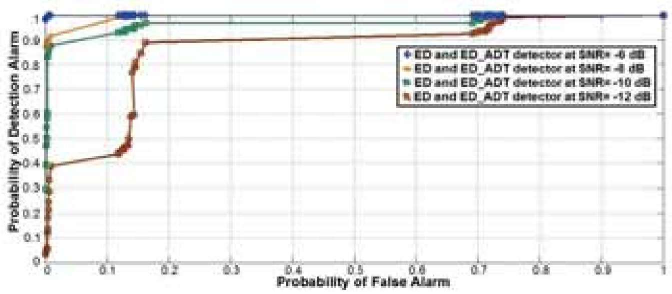

Figure 7: Receiver operating characteristics (ROC) curves for ED and ED_ADT based spectrum sensing detector for different SNR values

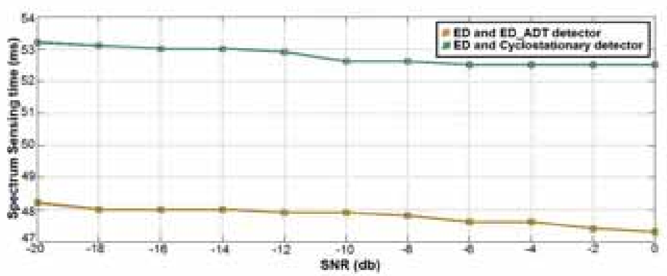

Figure 8: Spectrum sensing time vs SNR with N = 1000, QPSK modulation scheme and Rayleigh fading channel

M is the quantization decision and X denotes received signal energy by the CR user.

In Figure 2, a two-bit quantization method is used to divide the confused region into four equal quantization intervals as λ_2A-AB-BC-Cλ_1, where λ_2, A, B, C and λ_1 are sub-thresholds (ST) and their values are chosen as:

$$ST = \begin{cases} A = \lambda_2 + D \\ B = A + D \\ C = B + D \\ \lambda_1 = C + D \end{cases} \tag{9}$$

M is the quantization decision and X denotes received signal energy by the CR user.

In Figure 2, a two-bit quantization method is used to divide the confused region into four equal quantization intervals as λ_2A-AB-BC-Cλ_1, where λ_2, A, B, C and λ_1 are sub-thresholds (ST) and their values are chosen as:

$$ST = \begin{cases} A = \lambda_2 + D \\ B = A + D \\ C = B + D \\ \lambda_1 = C + D \end{cases} \tag{9}$$

$$D = \frac{(Upper\ bound - Lower\ bound)}{No.\ of\ Quantization\ intervals}$$

$$= \frac{(\lambda_1 - \lambda_2)}{4} \tag{10}$$

$$M = \begin{cases} 00, \lambda_2 < X \le A \\ 01, A < X \le B \\ 10, B < X \le C \\ 11, C < X < \lambda_1 \end{cases} \tag{11}$$

Using Equation 4, given the target false alarm probability $\overline{P_f}$, the threshold λ can be determined as:

$$\lambda = Q^{-1}\left(\overline{P_f}\right) \times \sqrt{2N\sigma_\omega^4} + N\sigma_\omega^2 \tag{12}$$

where $Q^{-1}()$ shows the inverse Gaussian tail probability Q-function. This assumes that the noise uncertainty in the wireless network environment is defined as $[1/\rho\sigma_\omega^2, \rho\sigma_\omega^2]$, where ρ is a constant parameter that computes the size of the uncertainty and $\rho > 1$.

In the adaptive threshold decision scheme, we have chosen two thresholds λ_1 and λ_2, where the value of the maximum noise variance shows the value of the upper threshold λ_1 and the value of the minimum noise variance shows the value of the lower threshold λ_2. Hence:

$$\lambda_1 = Q^{-1}\left(\overline{P_f}\right) \times \sqrt{2N\rho\sigma_\omega^4} + N\rho\sigma_\omega^2 \tag{13}$$

$$\lambda_2 = Q^{-1}\left(\overline{P_f}\right) \times \sqrt{2N/(\rho\sigma_\omega^4)} + N/(\rho\sigma_\omega^2) \tag{14}$$

If detected signals fall inside any one of the quantized intervals, the scheme will generate its respective decimal values (DV) as:

$$DV = \begin{cases} If\ M = 00, respective\ decimal\ value - 0 \\ If\ M = 01, respective\ decimal\ value - 1 \\ If\ M = 10, respective\ decimal\ value - 2 \\ If\ M = 11, respective\ decimal\ value - 3 \end{cases} \tag{15}$$

Equation 15 shows the decimal values (DV), which are compared with the threshold (λ) to make a local decision at a fixed P_f, i.e. 0 or 1. Outside the confused region the scheme will generate 0 or 1 depending on the signal's position.

Dual-Detectors System

Figure 3 shows the model of the proposed dual-detectors system with two energy detectors.

Figure 4 shows the internal architecture of the ED with single threshold *(γ)*. Here, the input PU-licensed signal is received by the square law device, which shows the detected signal energy *(X)* and compares it with the single threshold to make a final decision to determine whether the PU is present or not.

$$X = \frac{1}{N}\sum_{n=1}^{N} |x(n)|^2 \qquad (16)$$

The first-stage local decision rule *(LF)* used by the ED with single threshold is given by:

$$LF = \begin{cases} 1, \gamma \leq X \\ 0, X < \gamma \end{cases} \qquad (17)$$

If a signal is not detected in the first stage, then the second stage detector comes into the picture as shown in Figure 5. A square law device detects the signal and shows the signal energy *(X)*. After the square law device there are two sections, called upper section and lower section. In the upper section, if detected energy values *(X)* are greater than λ_1, it will show H_1 (signal present), or less than λ_2 show H_0 (signal absent). But, if the detected energy values *(X)* fall between λ_1 and λ_2 then it will follow the lower section and use the quantization method to generate respective decimal values (DV) as shown in Equation 15.

If the detected energy values (*X*) fall outside or between λ_1 and λ_2, using Equations 8, 11 and 15, the system will generates values as per the following equations:

$$m = \begin{cases} 0, X \leq \lambda_2 \\ 1, \lambda_1 \leq X \end{cases} \qquad (18)$$

$$n = \{DV, \lambda_2 < X < \lambda_1 \qquad (19)$$

where *m* and *n* are the output values of the upper part and lower part respectively. After that values of *m* and *n* are added using an adder.

$$Y = (m + n) \qquad (20)$$

Finally, the second-stage local decision (*LS*) is expressed using Equations 18, 19 and 20, which gives the final output of ED_ADT as follows:

$$LS = \begin{cases} 1, \lambda \leq Y \\ 0, Y < \lambda \end{cases} \qquad (21)$$

Equation 21 compares the resultant value *(Y)* to the threshold *(λ)*, which is maintaining the overall system probability of false alarms (P_f) 0 or 1. If *Y* is greater than *λ* a signal is present, otherwise it is absent.

Algorithm: The proposed dual-detectors for spectrum sensing

1: Given $\{x_1, x_2, x_3, \ldots, x_N\}$
2: Given $\{\gamma\}$
3: Given $\{\lambda_1, \lambda_2; \lambda\}$
4: Distribute uniformaly $\{\lambda_2, \lambda_1\}$
as $\{\lambda_2 < A < B < C < \lambda_1\}$
5: Define Range $R_0 = \{\lambda_2, A\}$, $R_1 = \{A, B\}$,
$R_2 = \{B, C\}$, $R_3 = \{C, \lambda_1\}$,
6: Values for Ranges n = {0,1,2,3} for
$\{R_0, R_1, R_2, R_3\}$
7: X = 0;
8: **for** i = 1,2,...,N
$X = X + x_i^2$;
endfor
9: **if** $X \geq \gamma$
$LF = H_1$;
else if $X \geq \lambda_1$
$m = H_1$;
else if $X \leq \lambda_2$
$m = H_0$;
else
for j = 0,1,2,3
if $X \in R_j$
n = j;
endif
endfor
10: Y = m+n;
11: **if** $Y \geq \lambda$
$LS = H_1$;
else
$LS = H_0$;
endif
endif

Final Analysis

In our system model, we assumed the total number of samples *(N)* is 1000, the SNR range varies from -20dB to 0dB, $P_f = 0.1$ and a QPSK modulation is considered in Rayleigh fading channel.

Figure 6 shows the comparative performance of the proposed scheme with the cyclostationary detections method (previous scheme). It is found that our scheme yields better results and the detection performance is improved by 12.9% at -8dB SNR.

Figure 7 shows the receiver operating characteristics (ROC) curves, which exhibit the relationship between sensitivity (probability of detection alarm) and specificity (probability of false alarm) [11] of a spectrum sensing method for different SNR values. This implies that when $P_f = 0.1$ and SNR = -10dB, the probability of detection is greater/closer to 0.9, which is the spectrum sensing requirement of the IEEE 802.22 [12].

Figure 8 shows the graph of spectrum sensing time versus SNR. The spectrum sensing time is the time taken by CR user to detect a licensed PU signal. Figure 8 shows that the proposed scheme requires less sensing time than with the previous scheme, and a shorter sensing time also increases throughput. It is observed that there is an inverse relation between spectrum sensing time and SNR. As SNR increases, the sensing time decreases. At -20dB SNR, the proposed scheme takes approximately 48.2ms for sensing, whilst the previous scheme requires around 53.2ms.

$$T = T_F + T_S \tag{22}$$

In Equation 22, T is the total spectrum-sensing time for a CR user. T_F and T_S are the first stage and second stage spectrum-sensing times of individual CR users respectively. ●

REFERENCES

[1] Ashish Bagwari, and Brahmjit Singh, "Comparative performance evaluation of Spectrum Sensing Techniques for Cognitive Radio Networks," 2012 Fourth IEEE International Conference on Computational Intelligence and Communication Networks (CICN-2012), pp. 98-105.

[2] onghong Zeng, Ying-Chang Liang, Anh Tuan Hoang, and Rui Zhang, "A Review on Spectrum Sensing for Cognitive Radio: Challenges and Solutions", EURASIP Journal on Advances in Signal Processing, vol. 2010, pp. 1-15, 2010.

[3] ina Maleki, Ashish Pandharipande, and Geert Leus, "Two-Stage Spectrum sensing for cognitive radios," IEEE conference on Acoustics Speech and Signal Processing (ICASSP), pp. 2946-2949, 2010.

[4] Shi-Qi Liu, Bin-Jie Hu, and Xian-Yi Wang, "Hierarchical Cooperative Spectrum Sensing Based on Double Thresholds Energy Detection," IEEE Communications Letters, Vol. 16, No. 7, July 2012, pp. 1096-1099.

[5] Chunyi Song, Yohannes D. Alemseged, Ha Nguyen Tran, Gabriel Villardi, Chen Sun, Stanislav Filin, and Hiroshi Harada, "Adaptive Two Thresholds based Energy Detection for Coopeartive spectrum sensing," in Proc. 2010 IEEE CCNC, pp. 1-6.

[6] A. Ghasemi and E. S. Sousa, "Collaborative spectrum sensing for opportunistic access in fading environments," in Proc. IEEE International symposium on New Frontiers in Dynamics Spectrum Access Networks, 8-11 Nov. 2005, pp. 131-136.

[7] H. Urkowitz, "Energy detection of unknown deterministic signals," In Proc. IEEE, vol. 55, no. 4, pp. 523-531, Apr. 1967.

[8] Miguel López-Benítez, and Fernando Casadevall, "Improved Energy Detection Spectrum Sensing for Cognitive Radio," In IET Communications, vol. 6, Issue 8, pp. 785-796, 09 July 2012.

[9] ZHANG Ling-ling, HUANG Jian-guo, and TANG Cheng-kai, "Novel Energy Detection Scheme in Cognitive Radio," IEEE conference on Signal Processing, Communications and Computing (ICSPCC), pp. 1-4, 2011.

[10] R. Tandra, and A. Sahai, "SNR Walls for Signal Detection," IEEE Jour. of Slected Topic in Sig. Proc., vol. 2, no.1, pp. 4–16, Feb. 2008.

[11] Tevfik Yucek, and Huseyin Arslan, "A Survey of Spectrum Sensing Algorithms for Cognitive Radio Applications," IEEE Communication Serveys and Toutorials, vol. 11, No. 1, First Quarter 2009, pp. 116-130, 2009.

[12] Tuan Do, and Brian L. Mark, "Improving Spectrum Sensing Performance by Exploiting Multiuser Diversity," Foundation of Cognitive Radio Systems, Prof. Samuel Cheng (Ed.), ISBN: 978-953-51-0268-7, pp. 119-140, March 2012.

FINITE-DIFFERENCE TIME-DOMAIN OF EQUI-DIMENSIONAL FORM

JINZU JI, FEILIANG LIU AND **PEILIN HUANG** FROM THE SCHOOL OF AERONAUTIC SCIENCE AND ENGINEERING AT BEIHANG UNIVERSITY, BEIJING, MAKE THE EQUATIONS USED IN CALCULATING POINT SOURCE RADIATION AND METAL SQUARE CYLINDER SCATTERING SIMPLER AND MORE CONCISE

Since first proposed by Yee in 1966, and over 40 years of development, Finite-Difference Time-Domain (FDTD) has become a powerful algorithm. It is widely used in the areas of electromagnetic field numerical calculation, including electromagnetic scattering and radiation, microwave device simulation, electromagnetic compatibility and so on.

FDTD can be used to analyze any type of media, including a dispersive, anisotropic, inhomogeneous medium that cannot be easily simulated by other frequency domain algorithms, such as the method of moments (MoM) or the finite element method (FEM). For example, water is a dispersive medium, having different light speeds at different frequencies. FDTD can easily simulate the dispersive characteristics – by using the absorbing boundary condition (ABC), FDTD can calculate an infinite number of area problems.

Unlike others, the FDTD algorithm transforms Maxwell's differential equation directly into difference equations by spatial and temporal discretization. (Difference equations relate to differential equations as discrete mathematics relates to continuous mathematics.) There is no need to incorporate a boundary condition between the different media; instead, the media's parameters such as permittivity, permiability, electric conductivity and magnetic conductivity should be assigned.

In this article, by modifying the representation of the electric and magnetic fields, they have the same dimension (see later on). Media parameters such as permittivity, permiability and electric and magnetic conductivity are also modified into a simpler form. The Maxwell differential equations are simplified and, as a result, the discretized equations also have a simpler form, easily applied to numerical algorithms.

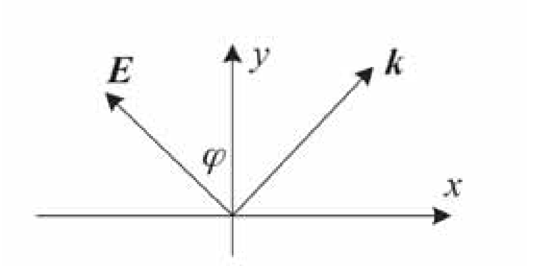

Figure 1: PML schematic of TE plane wave

The Equi-dimensional Form And Difference Scheme

First, we assume that the calculated area is filled with linear, homogeneous and isotropic (LHI) media. The time domain form of the electromagnetic field's curl equations can be written as follows:

$$
\begin{aligned}
\nabla\times\boldsymbol{E} &= -\mu\frac{\partial \boldsymbol{H}}{\partial t}-\sigma_m\boldsymbol{H}\\
\nabla\times\boldsymbol{H} &= \varepsilon\frac{\partial \boldsymbol{E}}{\partial t}+\sigma\boldsymbol{E}
\end{aligned}
\tag{1}
$$

where $\boldsymbol{E}$ is electric field strength (V/m), $\boldsymbol{H}$ is the magnetic field strength (A/m), ε is permittivity (F/m), μ is permeability (H/m), σ_m is magnetic conductivity ($\Omega\cdot$m) and σ is electric conductivity ($S\cdot$m). The curl equations can be rewritten as:

$$
\begin{aligned}
\nabla\times\left(\sqrt{\varepsilon}\boldsymbol{E}\right) &= -\sqrt{\varepsilon\mu}\left[\frac{\partial\left(\sqrt{\mu}\boldsymbol{H}\right)}{\partial t}+\frac{\sigma_m}{\mu}\sqrt{\mu}\boldsymbol{H}\right]\\
\nabla\times\left(\sqrt{\mu}\boldsymbol{H}\right) &= \sqrt{\varepsilon\mu}\left[\frac{\partial\left(\sqrt{\varepsilon}\boldsymbol{E}\right)}{\partial t}+\frac{\sigma}{\varepsilon}\sqrt{\varepsilon}\boldsymbol{E}\right]
\end{aligned}
\tag{2}
$$

Let $\boldsymbol{e}=\sqrt{\varepsilon}\boldsymbol{E}$, $\boldsymbol{h}=\sqrt{\varepsilon}\boldsymbol{H}$, $\bar{\sigma}_m=\sigma_m/\mu$, $\bar{\sigma}=\sigma/\varepsilon$, considering $c=1/\sqrt{\varepsilon\mu}$ where c is the wave speed, Equations 2 can be written in the form of:

$$
\begin{aligned}
c\nabla\times\boldsymbol{e} &= -\frac{\partial \boldsymbol{h}}{\partial t}-\bar{\sigma}_m\boldsymbol{h}\\
c\nabla\times\boldsymbol{h} &= \frac{\partial \boldsymbol{e}}{\partial t}+\bar{\sigma}\boldsymbol{e}
\end{aligned}
\tag{3}
$$

This is much more concise than Equation 2, and $\boldsymbol{e}$ and $\boldsymbol{h}$ have the same dimension $\sqrt{P}/L$, where P and L represent power and length respectively. The media are determined by $\bar{\sigma}_m$ and $\bar{\sigma}$, which have the same dimension 1/T, where T represents time.

There are two time harmonics: $e^{j\omega t}$ and $e^{-j\omega t}$, both used frequently by different authors. Different assumptions may require different formulae formats, but have the same physical meaning. Here we used $e^{j\omega t}$, where ω is angular frequency, and the curl equations in frequency domain are:

$$
\begin{aligned}
c\nabla \times \boldsymbol{e} &= -j\omega\left(1 - j\,\tilde{\sigma}_m/\omega\right)\boldsymbol{h} \\
c\nabla \times \boldsymbol{h} &= j\omega\left(1 - j\,\tilde{\sigma}/\omega\right)\boldsymbol{e}
\end{aligned}
\tag{4}
$$

where $\tilde{\sigma}_m/\omega$ and $\tilde{\sigma}/\omega$ represent the imaginary part of permittivity and permeability.

The Difference Form Of The Curl Equations

The grid size of FDTD is δ, wavelength is λ and time step is Δt. Space and time grid factors are defined as $f_s = \lambda/\delta$ and $f_t = \delta/(c\Delta t)$. Electric and magnetic fields are sampled in the centres and edges of the Yee's grid respectively. Take for example the x component, the electric and magnetic fields at the sampling points are denoted by Equations 5 and 6:

$$e_x^n(i,j,k) = e\left[(i+1/2)\delta, j\delta, k\delta, n\Delta t\right] \tag{5}$$

$$h_x^n(i,j,k) = h\left[i\delta, (j+1/2)\delta, (k+1/2)\delta, (n+1/2)\Delta t\right] \tag{6}$$

where i, j, k represent the spatial number and n represents the temporal number.

The electric field of the difference scheme can be written as Equation 7:

$$
\begin{aligned}
e_x^{n+1}(i,j,k) = \mathrm{ca}\cdot e_x^n(i,j,k) + \mathrm{cb}\cdot\big[h_z^n(i,j,k) - \\
h_z^n(i,j-1,k) - h_y^n(i,j,k) + h_y^n(i-1,j,k)\big]
\end{aligned}
\tag{7}
$$

where ca and cb are defined by conductivity, time gird factor and temporal step, which are shown in Equations 8 and 9:

$$\mathrm{ca} = \frac{1 - \tilde{\sigma}\Delta t/2}{1 + \tilde{\sigma}\Delta t/2} \tag{8}$$

$$\mathrm{cb} = \frac{1}{f_t}\frac{1}{1 + \tilde{\sigma}\Delta t/2} \tag{9}$$

The magnetic field from the difference scheme can be written as Equation 10:

$$
\begin{aligned}
&h_x^{n+1}(i,j,k) = \mathrm{cp}\cdot h_x^n(i,j,k) \\
&-\mathrm{cq}\cdot\left[e_z^n(i,j+1,k) - e_z^n(i,j,k) - e_y^n(i+1,j,k) + e_y^n(i,j,k)\right]
\end{aligned}
\tag{10}
$$

where cp and cq are:

$$\mathrm{cp} = \frac{1 - \tilde{\sigma}_m\Delta t/2}{1 + \tilde{\sigma}_m\Delta t/2} \tag{11}$$

$$\mathrm{cq} = \frac{1}{f_t}\frac{1}{1 + \tilde{\sigma}_m\Delta t/2} \tag{12}$$

When the electric and magnetic conductivity are all zero, namely $\tilde{\sigma} = \tilde{\sigma}_m = 0$, the coefficient of the difference equation appears to be in a very simple form:

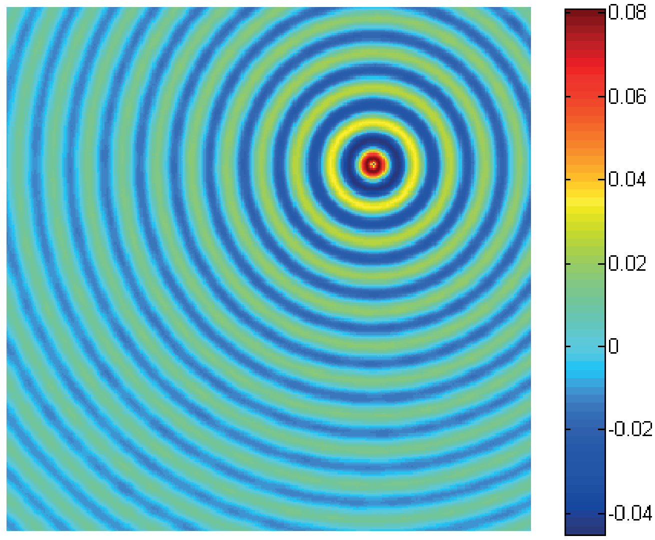

Figure 2: Results of line source radiation with second order Mur ABC

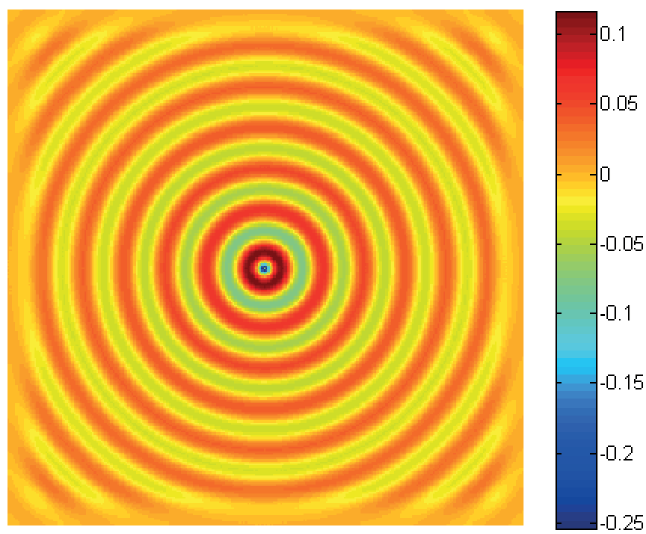

Figure 3: Results of line source radiation with PML ABC

$$\mathrm{ca} = 1, \mathrm{cb} = 1/f_t, \mathrm{cp} = 1, \mathrm{cq} = 1/f_t \tag{13}$$

The Exponential Difference Form

Taking the e_x component of the transverse electric (TE) wave as an example, the differential equation is:

$$\frac{\partial e_x}{\partial t} + \tilde{\sigma} e_x = c\frac{\partial h_z}{\partial y} \tag{14}$$

We can calculate the $n+1$ step field with:

$$e_x^{n+1}\left(i+\frac{1}{2},j\right)=e_x^n\left(i+\frac{1}{2},j\right)e^{-\tilde{\sigma}\Delta t}+\frac{c}{\tilde{\sigma}}\left(1-e^{-\tilde{\sigma}\Delta t}\right)\frac{\partial h_z}{\partial y}\bigg|^n \quad (15)$$

The partial derivative of y is discretized as:

$$\frac{\partial h_z}{\partial y}\bigg|^n=\frac{1}{\delta}\left[h_z^n(i,j)-h_z^n(i,j-1)\right] \quad (16)$$

The time step Δt is expressed by the space and time grid factor:

$$\Delta t=\frac{\delta}{cf_t}=\frac{\lambda}{cf_s f_t}=\frac{1}{f_s f_t f} \quad (17)$$

where f is frequency. Let $\tilde{\sigma}_f=\tilde{\sigma}/(f_t f_s f)$, then the difference Equation 15 is written as:

$$e_x^{n+1}(i,j)=e_x^n(i,j)e^{-\tilde{\sigma}_f}+\frac{1}{f_t}\frac{1}{\tilde{\sigma}_f}\left(1-e^{-\tilde{\sigma}_f}\right)\left[h_z^n(i,j)-h_z^n(i,j-1)\right] \quad (18)$$

when $\tilde{\sigma}_f=0$, $(1-e^{-\tilde{\sigma}_f})/\tilde{\sigma}_f=1$ and the exponential difference form degrades to the classic form.

In setting up the Perfectly Matched Layer (PML) parameters, such expressions will bring great convenience.

Discrete Form of The Absorbing Boundary Condition (ABC)

The discrete form of the Absorbing Boundary Condition (ABC) expressed in equi-dimensional form also shows a symmetric and simple style. Take Mur and PML as an example. Taking transverse magnetic (TM) wave for example in the boundary $x=0$, the differential equation of second order Mur ABC is:

$$\frac{\partial e_z}{\partial x}-\frac{1}{c}\frac{\partial e_z}{\partial t}-\frac{1}{2}\frac{\partial h_x}{\partial y}=0 \quad (19)$$

The corresponding difference form is:

$$\begin{aligned}e_z^{n+1}(i,j)&=e_z^n(i+1,j)+\mathrm{P}\left[e_z^{n+1}(i+1,j)-e_z^n(i,j)\right]\\&-\mathrm{Q}\left[h_x^n(i,j)-h_x^n(i,j-1)+h_x^n(i+1,j)-h_x^n(i+1,j-1)\right]\end{aligned} \quad (20)$$

where:

$$\mathrm{P}=\frac{c\Delta t-\delta}{c\Delta t+\delta}=\frac{1-f_t}{1+f_t} \quad (21)$$

and

$$\mathrm{Q}=\frac{1}{2}\frac{c\Delta t}{c\Delta t+\delta}=\frac{1}{2(1+f_t)} \quad (22)$$

Obviously, by using the equi-dimensional form, the corresponding coefficients of the calculation are very concise, as they are only associated with the time grid factor f_t and are dimensionless quantities.

PML Boundary Condition

Taking the TE wave for example, the related fields are h_z, e_x and e_y. In the PML absorbing medium the magnetic field component h_z is split into two sub h_{zx} and h_{zy}, that is $h_z=h_{zx}+h_{zy}$. Moreover, the Maxwell equations are:

$$\frac{\partial e_x}{\partial t}+\tilde{\sigma}_y e_x=c\frac{\partial\left(h_{zx}+h_{zy}\right)}{\partial y} \quad (23)$$

$$\frac{\partial e_y}{\partial t}+\tilde{\sigma}_x e_y=-c\frac{\partial\left(h_{zx}+h_{zy}\right)}{\partial x}, h_z=h_{zx}+h_{zy} \quad (24)$$

$$\frac{\partial h_{zx}}{\partial t}+\tilde{\sigma}_{mx}h_{zx}=-c\frac{\partial e_y}{\partial x} \quad (25)$$

$$\frac{\partial h_{zy}}{\partial t}+\tilde{\sigma}_{my}h_{zy}=c\frac{\partial e_x}{\partial y} \quad (26)$$

Considering the TE wave of Figure 1, the electric field's amplitude is e_0 and φ is the angle between the electric field and the y axis.

The parameters h_{zx0} and h_{zy0} are the amplitudes of magnetic field h_{zx} and h_{zy}, respectively. The field components are represented in Equation 27:

$$\begin{aligned}&e_x=-e_0\sin\varphi e^{j\omega(t-\alpha x-\beta y)}, e_y=e_0\cos\varphi e^{j\omega(t-\alpha x-\beta y)},\\&h_{zx}=h_{zx0}e^{j\omega(t-\alpha x-\beta y)}, h_{zy}=h_{zy0}e^{j\omega(t-\alpha x-\beta y)}\end{aligned} \quad (27)$$

By the method of Berenger, we can solve α and β in Equation 28:

$$\alpha=\frac{1}{cG}\left(1-j\frac{\tilde{\sigma}_x}{\omega}\right)\cos\varphi, \beta=\frac{1}{cG}\left(1-j\frac{\tilde{\sigma}_y}{\omega}\right)\sin\varphi \quad (28)$$

where:

$$\begin{aligned}&G=\sqrt{w_x\cos^2\varphi+w_y\sin^w\varphi}, w_x=\\&(\omega-j\tilde{\sigma}_x)/(\omega-j\tilde{\sigma}_{mx}), w_y=(\omega-j\tilde{\sigma}_y)/(\omega-j\tilde{\sigma}_{my})\end{aligned} \quad (29)$$

$\tilde{\sigma}_x=\tilde{\sigma}_{mx}, \tilde{\sigma}_y=\tilde{\sigma}_{my}$ $w_x=1, w_y=1$ and $G=1$ at any frequency.

Validation By Examples

The algorithm is validated by three numerical examples:

Line source radiation and second order Mur ABC

In this example, the grid size is $(-150:150, -150:150)$, $f_s = 20$ and $f_t = 1.5$. The location of the point source is $(60, 60)$ and frequency is 10GHz. Figure 2 is the electric field after 1000 time-step iterations, with field distribution in concentric circles, which shows that the outward wave is absorbed.

Line source radiation and second order PML ABC

In this example, the grid size is $(-125:125, -125:125)$ and the source locates at $(0, 0)$. The thickness of the PML absorbing layer is 20 grids. The electric and magnetic conductivity in the PML layer is of linear distribution, and $\bar{\sigma}_f = \bar{\sigma}_{mf} = 0.2$ at the outer side and $\bar{\sigma}_f = \bar{\sigma}_{mf} = 0$ at the inner side. The line source's frequency is 10GHz. The magnetic field after 1000-step iterations is shown in Figure 3.

In Figure 3, there is an electromagnetic wave propagating in the ABC area, but the intensity attenuates rapidly and there is almost no echo wave.

Scattering experiment of metal square column

Figure 4 shows the conductive square scattering using the second order Mur ABC in TM wave. The grid size is $(-150:150, -150:150)$ and $f_s = 20, f_t = 1.5$. Incident frequency is 10GHz. The target's edge is 0.06 meters. There are 40 grids between the connection boundary and the absorbing boundary. The scattering field was calculated at the incident angles of 0° and 45°. The electric field distribution after 1000 steps is shown in Figures 4 and 5.

It can be seen that the square in the centre is a conductive scatterer and the field is zero. The calculation area was divided into total field and scattered field.

New Form of Equations

When using FDTD to calculate the electromagnetic field, Maxwell's curl equations were rewritten in equi-dimensional form, which simplifies the manipulating process and makes the program more concise. The new form can be used in difference equations, absorbing boundary conditions, electromagnetic radiation, scattering and so on. The numerical examples confirm the effectiveness of the algorithm. ●

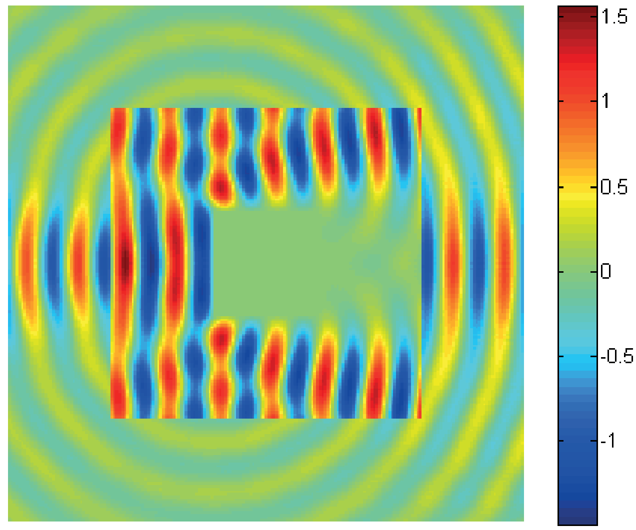

Figure 4: Metal square scattering at 0° incident

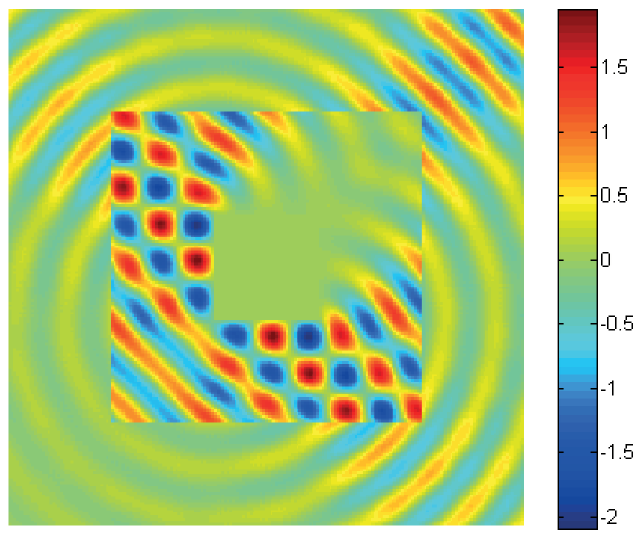

Figure 5: Metal square scattering at 45° incident

Harvard Engineering's latest product, EyeNut is a wireless control, management and monitoring solution for indoor lighting

TECHNOLOGICAL ADVANCES HAVE MADE INDOOR LIGHTING CONTROLS SIGNIFICANTLY MORE USER-FRIENDLY AND, FOR THE FIRST TIME, FACILITIES MANAGERS CAN CONFIGURE, CONTROL AND MONITOR SYSTEMS WITHOUT THE HELP OF A SPECIALIST ENGINEER. **DR ANDY DAVIES**, BUSINESS DEVELOPMENT MANAGER FOR INDOOR CONTROLS AT HARVARD ENGINEERING, GIVES THE FULL STORY

SIMPLIFYING LIGHTING CONTROLS

It is understood that using lighting controls can save energy and dramatically reduce greenhouse gas emissions. For most organisations, lighting represents the largest single item on their electricity bill – on average, 41% of all electricity consumption in commercial premises is due to lighting.

The International Energy Agency believes that if everyone used the most advanced energy-efficient LED lighting in combination with smart control and management systems, savings of up to 80% could be achieved across the board.

The amount of carbon dioxide produced globally from generating electricity for lighting is staggering – it is three times higher than all the emissions produced by aviation and the equivalent of 70% of the world's combined passenger vehicle CO2 output. Carbon dioxide is the largest of the trace gases and is currently responsible for creating 60% of the 'enhanced greenhouse effect'. This explains the urgency behind the government's target of reducing UK's greenhouse gas emissions by 80% from 1990 levels by 2050.

Using lights only when needed has the added benefit of decreasing internal heat gains, and reducing the need for air conditioning, which further contributes to energy and cost savings. Avoiding overlighting by using controls will save businesses millions in unnecessary electricity costs, as well as earning green credits towards BREEAM (Building Research Establishment Environmental Assessment Methodology) certification and the Carbon Reduction Commitment (CRC) Energy Efficiency Scheme.

The decision to install lighting controls should, therefore, be clear-cut. But take-up of lighting controls has been poor with reports showing only 25% of all the controllable lighting currently sold in Europe is being operated by anything more than an on/off switch. So what is the explanation?

Out of Control

One main reason why lighting controls have been given the cold shoulder is that current technology is complicated and expensive to implement.

Traditional controls can generally be divided into two categories: those integrated with Building Automation Systems (BAS), and dedicated lighting systems, such as DALI (Digital Addressable Lighting Interface) or Analogue 1–10V control, for dimming. These may be linked to several energy-saving strategies at once, e.g. time scheduling and scene setting, where different lighting scenarios are used to suit the activity taking place at a particular time to avoid overlighting.

Optimising the configuration of a control system can be challenging and usually requires a specialist engineer to carry it out. Add to that the fact that installing lighting controls in existing premises is disruptive and costly, because of the need to re-wire (which can interfere with existing building infrastructure), and it's easy to understand the reluctance of facility managers to make such a significant investment, especially when building use can alter rapidly and changing patterns of office working mean that spaces are used more flexibly. The importance of providing energy-saving solutions in existing buildings is highlighted by reports that estimate that 80% of the buildings which will be used in 2050 have already been built.

Industry-Changing Technology

New technology is emerging on the market that provides solutions to these key challenges while giving proven savings of up to 40%, on top of the benefits gained by switching over to LED lights (which is desirable but not mandatory). Such a technology heralds a new era for lighting controls and a hope that their use will – at last – become mainstream.

The new controls are wireless and don't require the services of a specialist engineer. They use GPS and radio frequency identification (RFID) to operate lights individually, in groups or throughout the entire infrastructure, and the system is capable of controlling 500 light-points from one wireless gateway, compared to DALI's capability of just 64.

For the first time it will be possible to operate lights for multiple buildings or multiple sites from a single computer hub. This means, for instance, that the facilities manager of a large supermarket


Harvard Engineering's EyeNut product incorporates technology adapted from the company's award-winning system for street lights, LeafNut

can choose to control the lighting for all its stores from one centre to achieve energy and maintenance savings. Being in full control of energy spend puts facility managers in the driving seat and one step ahead of mandatory government-required energy audits. By December 5th 2015, every large enterprise in the UK will, by law, have to undertake an energy audit that must be repeated every four years, in line with the European Union Energy Efficiency Directive.

These advances have been made possible by technological developments in wireless, networked, control systems, combined with innovations in the software user interface. The system uses the secure, open-protocol Zigbee mesh network, designed for low data-rate and low-power applications, and provides robust protection against communication breakdown between devices on the network. A Zigbee-network enabled LED driver is small, compact and presents no additional installation challenges.

Technological developments have also made comprehensive levels of data monitoring and analysis possible. Users can monitor the performance of lights throughout the system, collect energy consumption data, see the dim status of each light and predict lamp failure.

User-Friendly Controls

One of the most time-consuming processes in setting up traditional lighting control systems is adding each light to the network. The new technology allows luminaires to be scanned in very simply using an RFID scanner, and these lights are subsequently clearly visible on the Graphic User Interface (GUI), or dashboard, where they are mapped onto an imported image of the building layout. This makes it very easy to identify the status of all lights and to dim or switch them off accordingly. Lights can be operated individually or in groups, created, controlled and managed by facility managers. By implementing a number of indoor lighting strategies simultaneously, such as daylight harvesting, dimming, time scheduling and scene setting, a site's energy costs and carbon footprint can be significantly reduced.

The technology works in conjunction with other control gear, such as time switches and photocell sensors, which ensure that lights only come on at a level necessary to augment natural daylight. It also connects with Passive Infrared (PIR) detectors to switch lights on and off or dim them, depending on occupancy. This is especially useful in intermittently used areas such as corridors, restrooms and storerooms to either dim or switch lights off altogether.

The system integrates with existing building management systems to collect occupancy data and with fire-alarm systems so that lights respond to emergency situations. ●

FIRST VENTURE

A 4,500m^2 department store, part of a multinational chain, was looking to upgrade its lighting. It analysed the new technology to see what savings could be achieved. The store found that a 40% reduction in energy bills could be made, in addition to the savings generated by using LEDs.

The store was looking to install lighting controls to its already existing LED lighting scheme – easily achievable given the wireless nature of the new technology. It was advised that a number of lighting control strategies should be adopted within the store, which would all be managed from one central computer and would allow for sophisticated lighting displays.

Sales floors could be divided into zones, separated by aisle areas. Within each of these zones, ambient lighting, central accent lighting and perimeter accent lighting of vertical surfaces would then be controlled independently as could lights in aisles, stairwells and entrance areas. Occupancy sensors were also recommended to measure footfall by floor and zone and accent lighting which can be selectively dimmed to create ambiance at various times.

The system's profiling feature, accessed through the GUI, would enable accent lighting to be switched off and ambient lighting to be dimmed during cleaning and stocking. Windows could also be fitted with daylight sensors so that lighting could be dimmed or switched off in sunshine.

Thanks to the new technology's RFID functionality, the store would be able to bypass the usually arduous task of recognizing and addressing individual units on the network, long associated with existing lighting control schemes. Staff could simply scan in each luminaire using a RFID scanner or app on a tablet or smartphone, speeding up the process and adding flexibility to allow for changing lighting schemes.

Following the first three months of operation, the store managers found that the store would reduce electricity consumption from 330kWh a day to 1,500kWh, indicating a rewarding two-year payback on investment.

A LOW-COST AND HIGHLY RELIABLE AMPLITUDE MODULATOR DESIGN FOR PC-BASED PCI PLUG ULTRASONIC PULSER RECEIVER BOARDS

DR AHMET TURAN ÖZDEMIR FROM ERCIYES UNIVERSITY IN TURKEY PRESENTS A NON-INVASIVE TESTING TECHNIQUE FOR DETERMINING THE INTEGRITY OF A MATERIAL OR QUANTITATIVELY MEASURING ITS DESIRED CHARACTERISTICS WITHOUT DAMAGING IT

Non-Destructive Evaluation (NDE) is a non-invasive testing technique used for determining the integrity of materials or for quantitatively measuring their desired characteristics without damaging them. Moreover NDE techniques can be used to detect deformed areas, cracks, porosity and leaks, to characterize structures, measure dimensions and determine locations.

There are many NDE techniques around, such as visual inspection, tap testing, laser interferometry, thermography, x-rays, magnetic particles, acoustic emission, liquid penetrant, flux leakage, microwave, eddy current etc. However, ultrasonic non-destructive evaluation or ultrasonic testing (UT) is one of the most preferred inspection techniques in the field of composite material testing.

Ultrasonic Non-Destructive Testing

Through Transmission (TT) is the most common UT technique used for composite material inspection in the aerospace industry. A TT system consists of a pulser, digitizer, transmitter transducer and receiver transducer. Figure 1 shows a PCI plug TT system with its peripherals. The aim of the TT method is to carry ultrasonic waves between the transmitter and receiver transducers. The inspected material is placed between these transducers and the measured signals on the digitizer side are used to monitor the material's characteristics.

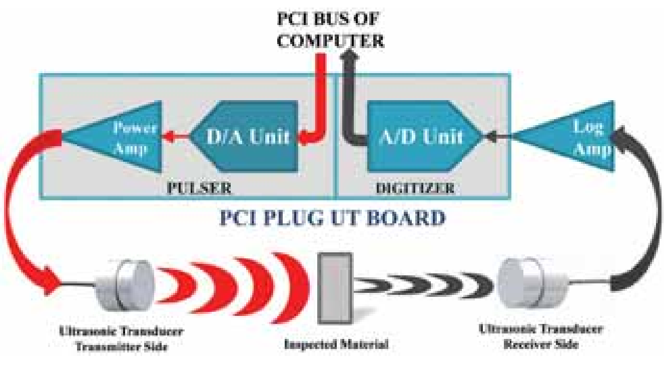

Figure 1: Basic configuration of a PCI plug TT system

A logarithmic amplifier is an optional peripheral needed on the digitizer side when the inspected material is thick, as thick composite materials (> 4cm honeycomb composites) are highly attenuative. The gap between the minimum and maximum signal amplitudes increases with attenuation. If the ultrasonic signal attenuation is too drastic, it is impossible to keep the amplitude variation within limits of the digitizer's analog-to-digital converter (ADC), because its sensitivity is generally 2V and this range can be easily exceeded. Figure 2 shows the typical relationship between the input and output signal of a logarithmic power amplifier.

The logarithmic power amplifier detects the burst envelope and produces logarithmic response as a function of the input voltage. A sinusoidal input signal consists of five different amplitude levels: 1mV, 10mV, 100mV, 1V and 10V (see Figure 2). The input signal varies from 0 to 10V peak voltage; however, the amplifier output varies from 0.1V to 1.53V. The amplifier output's slope is 0.2441V, which is ten times the voltage difference of the amplifier input. The 1mV and 10mV sinusoidal signals cannot be shown in the figure because of the linear graphical representation of the amplitude axis. The amplifier response was produced in Matlab environment.

The output signal of the logarithmic power amplifier is an envelope function of the burst pulses that becomes a DC signal level. The amplifier output cannot be read if the sampling unit has a high-pass or band-pass filter. The high- and band-pass filters need at least one frequency threshold, and it usually starts from 0.6MHz in PCI plug UT boards.

TT tests can be performed in an immersion tank, or with a water squirter or air scanning systems. Air is a highly attenuating medium, therefore large amplitude losses appear in the ultrasonic waves in the air. However, water is a good medium that carries ultrasonic waves between transmitter and receiver transducers with small losses.

In this work, a water squirter scanning system was used to carry ultrasonic waves (see Figure 3). There are two nozzles in the figure; the one on the left covers the piezoelectric transmitter transducer and the one on the right covers the piezoelectric receiver transducer.

PCI Plug UT Boards On The Market

Digitizer and pulser units can be separate or integrated. There are many integrated PCI plug UT boards available on the market; some are shown in Table 1. All of these boards have a band-pass filter on their digitizer side. Only the TB 1000 makes it possible for a user to disable the filtering and to read DC signals. This limitation becomes problematic when logarithmic amplification is needed in the TT system, because the amplifier output becomes a DC signal if the logarithmic amplification is made by a logarithmic power amplifier, and a converter unit is needed to read the amplifier output of UT boards on the market. Because of this problem, a cheap and reliable amplitude modulator has been designed. This modulator is necessary when using fast logarithmic power amplifiers with digitizer units with built-in filters.

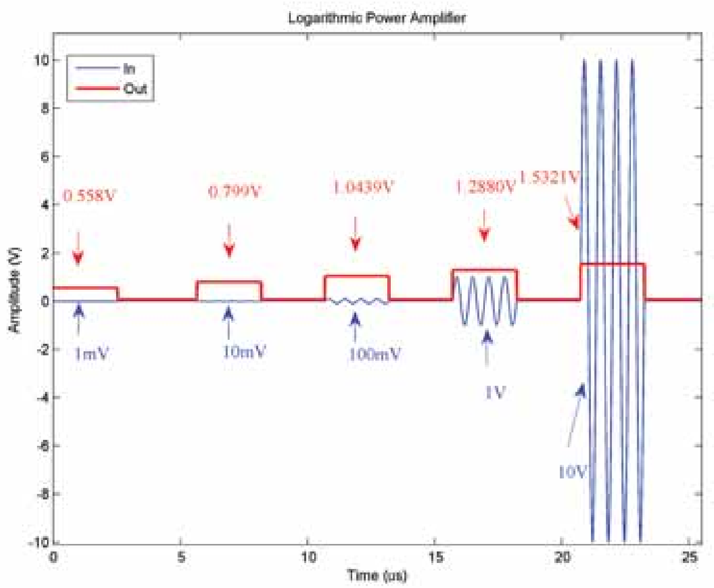

Figure 2: Potential power savings for different network standards

Amplitude Modulator Unit

In this work, an amplitude modulator was designed to modulate the logarithmic power amplifier output with the desired carrier frequency. Figure 4 shows the modulator simulation results. A 100kHz sinusoidal signal (red) is modulated by a 5MHz square wave (green) and an amplitude modulated signal is achieved (blue). In this circuit, Analog Devices's AD8036A low-distortion, wide-bandwidth, voltage feedback clamp amplifier was used as a modulator. The AD8036A input resistance is 150kΩ and output resistance is 0.3Ω. Its bandwidth is typically 240MHz and slew rate 1200V/µs. It is a very fast amplifier; its rise and fall times are 1.4ns for $V_{out} = 0.5V$ step and 2.6ns for $V_{out} = 4V$ step.

The modulator circuit schematic is shown in Figure 5. LTC1799 is an oscillator IC used for carrier frequency generation. This IC can generate square waves up to 33MHz. This is a sufficient range to generate ultrasonic waveforms, since 1, 2.5 and 5MHz are the preferred frequencies in the TT inspection method.

The LTC1799 is supplied in a +3.1V and -1.9V supply configuration, which helps produce a symmetric square wave in the 5V range. The positive supply voltage is larger than the negative one because the modulated signal logarithmic power amplifier output varies in the positive scale, and the amplifier's non-inverting input was used for modulation. Resistors R7 and R8 were chosen to be 274Ω since this configuration results in unity amplifier gain. Impedance matching is by resistor R9, because

Company	Device
Sofratest	SFT-4001H
Socomate	PC-RCPP7101
Ultrasonic Science	PM30
Mistras	ADIPR 1210
Us Ultratek	DSPUT 5000
Matec	TB 1000

Table 1: Some of PCI Plug pulser and receiver boards available on the market

Unit	Channel 1 (1MHz)	Price	Unit	Channel 2 (5MHz)	Price	Unit	Power Supply, Box and PCB	Price
1	AD8036A	9.99	1	AD8036A	9.99	1	24V to ±12V	40.19
1	LTC1799	4.99	1	LTC1799	4.99	1	LT1175	5.52
1	200kΩ Trimmer	4.94	1	200kΩ Trimmer	4.94	1	MIC5239-5	3.06
2	SMA Connector	4.80	2	SMA Connector	4.80	4	10uF 16V Tantal	0.75
1	1kΩ Trimmer	1.65	1	1kΩ Trimmer	1.65	2	100nF Capacitor	0.10
1	10uF 16V Tantal	0.75	1	10uF 16V Tantal	0.75	3	300Ω Bead	0.10
1	100nF Capacitor	0.10	1	100nF Capacitor	0.10	1	Aluminium Box	18.80
9	Resistors	0.10	9	Resistors	0.10	1	PCB	5.00
EACH UNIT		32.92			32.92			76.07
TOTAL								$ 141.91

Table 2: List of electronic components and hardware costs

Figure 3: A water squirter system

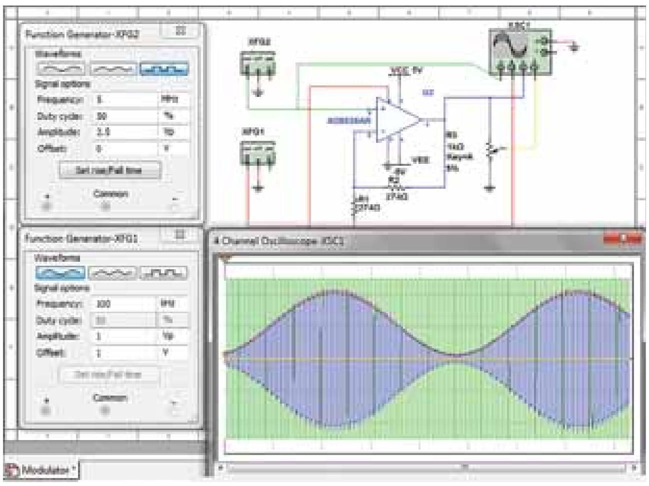

Figure 4: Modulator circuit simulation results

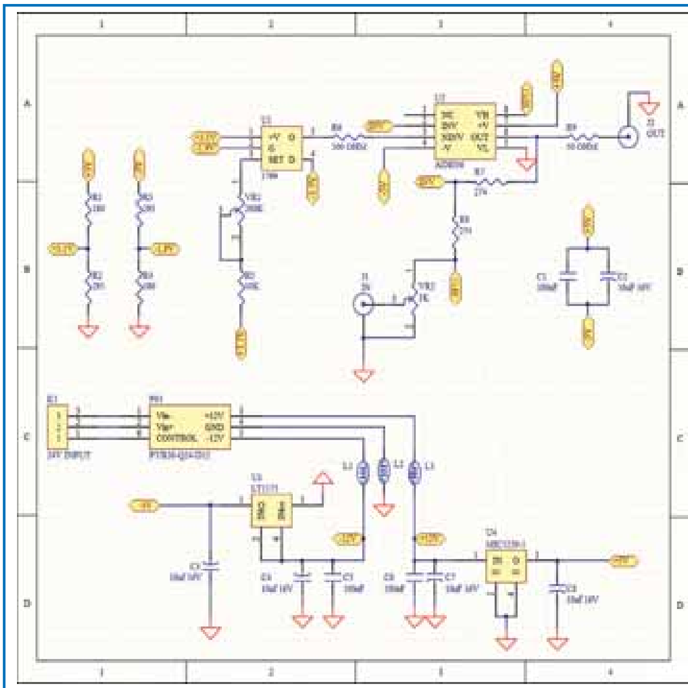

Figure 5: Modulator unit schematic diagram

this resistor should be the same as the digitizer input impedance, generally 50Ω. Resistors R1, R2, R3 and R4 are a voltage-divider tree. PS1 is a 24V to ±12V DC-to-DC converter that feeds two regulator units: MIC5239 (+5V LDO) and LT1175 (-5V LDO). The reason for selection of 24V input voltage is the availability of 24V in industrial areas.

Figure 6 shows the test setup of the modulator unit. The modulator input signal was produced by a signal generator. The input and output of the modulator unit were measured with a dual-channel 500MHz oscilloscope. The 200kHz sinusoidal signal was applied to the modulator unit, which then modulated this signal with a 5MHz square wave.

The input and output signal waveforms are shown in Figure 6. There are four oscilloscope screenshots in Figure 6; channel A shows the input and channel B shows the output of the modulator. The 200kHz sinusoidal, square wave and triangle input and output signal waveforms are shown in Figures 6a, b and c respectively. Figure 6d shows the logarithmic power amplifier output (red) and its modulated output (blue). The logarithmic power amplifier amplifies 1kHz signal bursts, and the modulator modulates the output of the amplifier with a 5MHz square-wave.

Results

The modulator circuit has been used for more than eighteen months without any issues at the Turkish Aerospace Industries inspection department on a 10-axis ultrasonic scanning system. The modulator is very reliable and has been used with the US Ultratek DSPUT 5000 PCI plug ultrasonic pulser and receiver board. This board and modulator have two channels: one for 1MHz and the other for 5MHz. Figure 7 shows the hardware test setup, while Figure 8 shows the modulator's PCB in its aluminum case.

The modulator's power consumption is 3.36W or 140mA current consumption at 24V input voltage. The cost of the modulator unit is given in Table 2. Two channel modulator unit costs $141.91 from DigiKey.

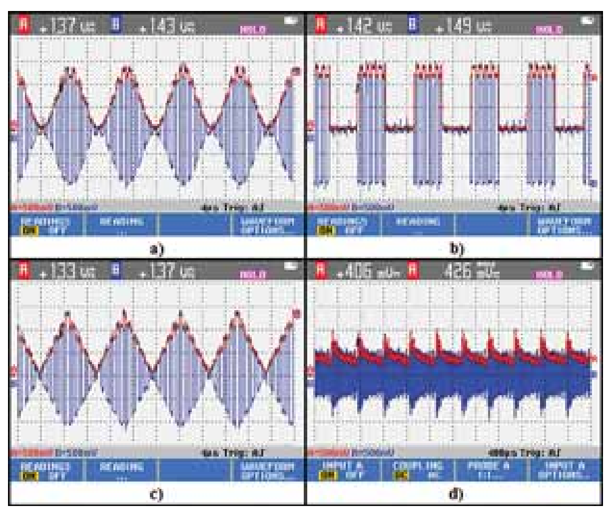

Figure 6: Oscilloscope screenshots

Figure 7: Test setup

In an ultrasonic inspection system, reliability is very important because 120dB signal attenuation is measured with a 2V ADC range. Therefore, the signal responses of all units must be stable, otherwise each inspection may not give results with the same characteristics. These inspection systems are certified each year, where the signal integrity is expected to be stable. Users must be aware of environmental noises, such as switch-mode power supplies, electric motors and large machines, that can interfere with ultrasonic signalling. Therefore, the scanning system and instrumentation hardware must be isolated from these noise sources, and calibration must be performed as soon as any hardware modification is made. ●


Figure 8: Modulator PCB

AUTONOMOUS NAVIGATION
FOR A QUADROTOR AIRCRAFT

WEI LIU, KAI HE AND **QUN GAO** FROM THE SCHOOL OF INFORMATION AND ELECTRONICS ENGINEERING AT THE SHANDONG INSTITUTE OF BUSINESS AND TECHNOLOGY IN YANTAI, CHINA, PRESENT A FLIGHT CONTROL SYSTEM FOR A QUADROTOR AIRCRAFT

We designed a flight control system that uses attitude, height and position sensor information to control unmanned flight of a quadrotor aircraft. The quadrotor structure has the shape of a cross, with a rotor at each of the four ends.

The rotors are divided into two groups: one group (rotors 1 and 3) rotates counter-clockwise, and the other group (rotors 2 and 4) rotates clockwise. By adjusting the rotor speed to change the flight attitude, the quadrotor aircraft can achieve vertical takeoff, landing, pitch, roll, yaw and lateral movement. The arrangement is shown in Figure 1.

The Control System

The control system of the quadrotor aircraft consists of a CPU, motor, sensors and power supply. The host CPU is the R5F100LEA device from Renesas Electronics. Four MOS transistors are used to drive four small DC motors. The sensor circuitry includes MPU6050 (3-axis gyroscope and 3-axis accelerometer), HMC5883L (magnetic sensor), BMP085 (pressure sensor) and a tracking sensor. Power is from a 3.7V power supply with 500mAh lithium battery. The overall system architecture is shown in Figure 2.

> "By adjusting rotor speed to change the flight attitude, the quadrotor aircraft can achieve vertical takeoff, landing, pitch, roll, yaw and lateral movement

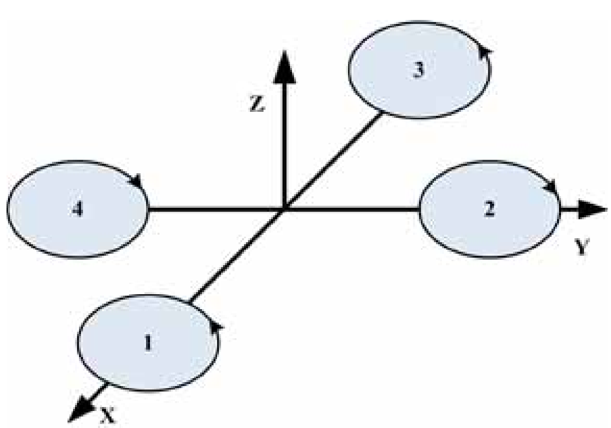

Figure 1: Schematic diagram of a quadrotor aircraft

The R5F100LEA is a high-performance 16-bit microcontroller with a large number of on-chip peripherals, including a 12-channel 8/10-bit A/D converter, a 2-channel I2C interface and a 2-channel DMA (Direct Memory Access) controller. A built-in 16-bit timer can output 8-channel PWM (Pulse Width Modulation) signals. A 2-channel timer can be used to generate a pulse with any period and duty cycle. By extending the PWM function and using the multiple slave channels, several PWM waveforms with different duty cycles can be created. As such, the R5F100LEA chip can output four PWM signals with different duty cycles to drive the four DC motors at any speed.

Interfacing the MPU6050 and CPU

The MPU6050 is the world's first motion-processing solution with integrated 9-axis sensor using a field-proven motion-fusion engine for tablet applications, game controllers and other consumer devices. The MPU6050 has an embedded 3-axis gyroscope, a 3-axis accelerometer and a DMP (Digital Motion Processor) hardware accelerator engine with an auxiliary I2C port which interfaces with third party digital sensors. An on-chip 1024-byte FIFO (First Input and First Output) buffer helps lower the system's power consumption by allowing the processor to read sensor data in bursts and then enter a low-power mode when the MPU is collecting more data. The interface circuit of MPU6050 and R5F100LEA is shown in Figure 3.

It can be seen that pins CLKIN, FSYNC and AD0 of MPU6050 connect to ground. The serial data pin SDA and serial clock pin SCL are connected to pins SDA01 and SCL01 of the CPU. The interrupt signal INT connects to INTP11. At first, CPU sends a command to MPU6050 via the I2C bus. When 6-axis data is ready, MPU6050 sends an interrupt signal to the CPU, which responds and reads the sensor data.

In a generalized I2C interface implementation, the attached devices can be a master or a slave. The master device puts the slave address on the bus, and the slave

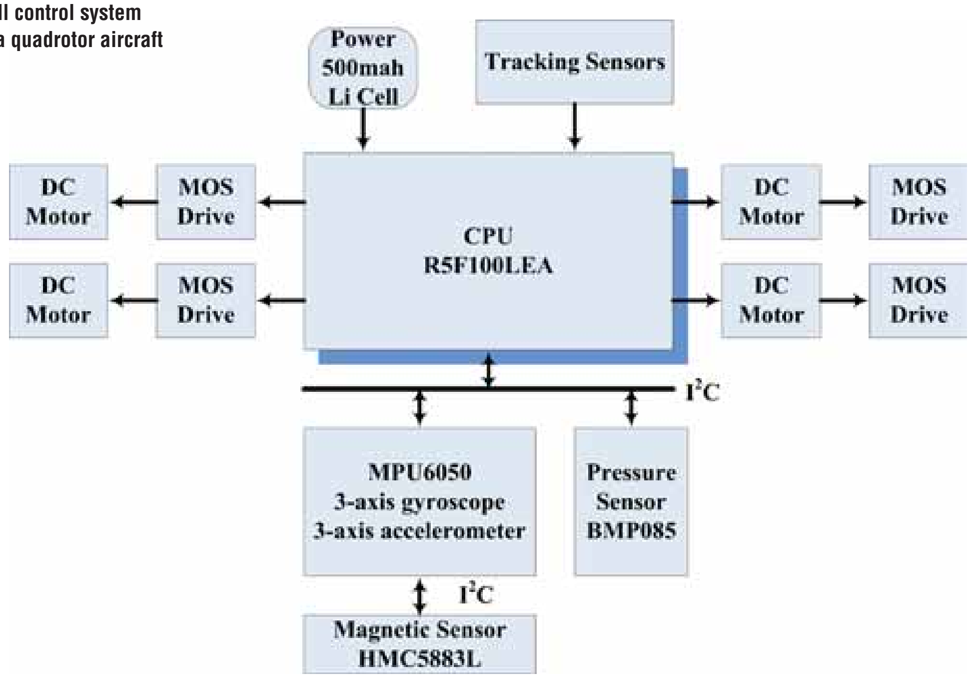

Figure 2: Overall control system architecture of a quadrotor aircraft

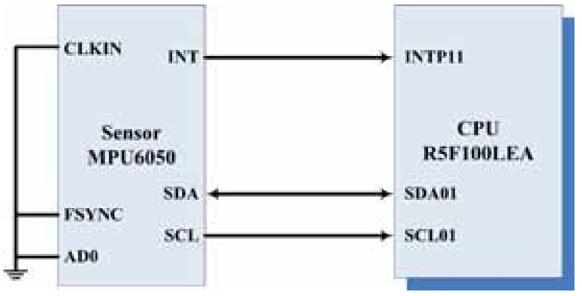

Figure 3: MPU6050 and CPU interface design

Figure 4: Our quadrotor aircraft design

device with the matching address acknowledges the master. The MPU6050 always operates as a slave when communicating with the CPU, which thus acts as a master.

The SDA and SCL lines typically need pull-up resistors to VDD. Maximum bus speed is 400kHz.

Design Of Autonomous Navigation

In general, the attitude measurement system comprises a 3-axis gyroscope, 3-axis accelerometer and 3-axis magnetometer, which assess the quadrotor aircraft's position and orientation. The difference between the expected and calculated values of Euler angles for the attitude acts as input to the PID controller, which then corresponds to the speed of the motors.

The physical picture of our quadrotor aircraft is shown in Figure 4. ●

THIS SERIES PRESENTS SOME SIMPLE ARDUINO PROJECTS. ARDUINO IS AN OPEN-SOURCE ELECTRONICS PROTOTYPING PLATFORM, BASED ON FLEXIBLE, EASY-TO-USE HARDWARE AND SOFTWARE

An LED Fade Sketch for the Arduino

BY **JOHN NUSSEY**

In this Arduino sketch, an LED can be made to fade on and off, with some additional hardware:

- An Arduino Uno;
- Breadboard;
- An LED;
- A resistor (greater than 120 ohms);
- Jumper wires.

It's always important to make sure the circuit is not powered while changes are being made to it, as incorrect connections can be easily made, potentially damaging the components.

This circuit is very simple, with pin 9 being the main one used, as it is capable of Pulse Width Modulation (PWM), applied to fade the LED. However, pin 9 also requires a resistor to limit the amount of current supplied to the LED. On pin 13, this resistor is already included on the Arduino board itself.

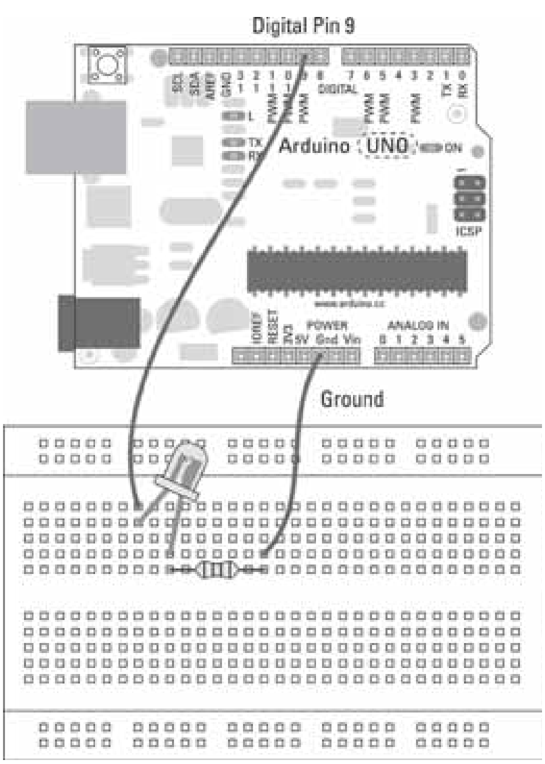

Figure 1: Pin 9 is connected to a resistor and an LED and then goes back to ground

Figure 1 shows the simple circuit connections. The digital pin (pin 9) is connected to the long leg (anode) of the LED; the short leg (cathode) connects to the resistor which goes to ground, GND. In this circuit, the resistor can be either before or after the LED.

It is good practice to colour-code the circuits, using various colours to distinguish one type of circuit from another, keeping things clear and making problem solving much easier. The most important areas to colour code are power and ground. These are nearly always coloured red and black, respectively, but may occasionally be seen as white and black as well.

The other type of connection is the signal wire, which sends and receives electrical signals between the Arduino and the components.

After the circuit is assembled, the appropriate software is needed to use it. From the Arduino menu, choose File>Examples>01.Basics >Fade to call up the Fade sketch. The complete code for the Fade sketch is as follows:

```
/*
 Fade
 This example shows how to fade an LED on pin 9
 using the analogWrite() function.
 This example code is in the public domain.
 */
int led = 9; // the pin that the LED is attached to
int brightness = 0; // how bright the LED is
int fadeAmount = 5; // how many points to fade the LED
by
// the setup routine runs once when you press reset:
void setup() {
 // declare pin 9 to be an output:
 pinMode(led, OUTPUT);
}
// the loop routine runs over and over again forever:
void loop() {
 // set the brightness of pin 9:
 analogWrite(led, brightness);
 // change the brightness for next time through the loop:
 brightness = brightness + fadeAmount;
 // reverse the direction of the fading at the ends of the
fade:
```

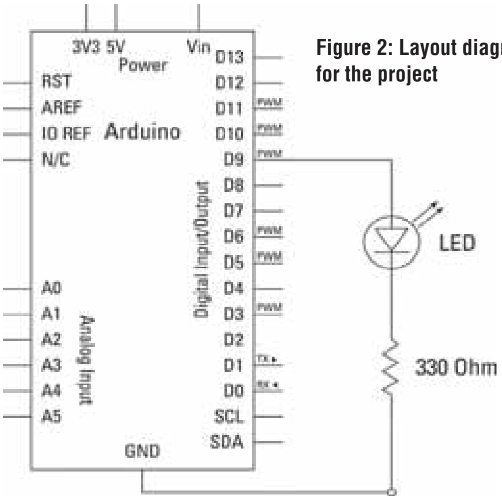

Figure 2: Layout diagram for the project

WIN THE 'ARDUINO FOR DUMMIES' BOOK BY JOHN NUSSEY

John Nussey is a creative technologist based in London. He teaches interaction design and prototyping at the Goldsmiths College and the Bartlett School of Architecture among others. We have a couple of copies of this book to give away. To enter please supply your name, address and email to the Editor at svetlanaj@sjpbusinessmedia.com. The winner will be drawn at random and announced at the end of the series.

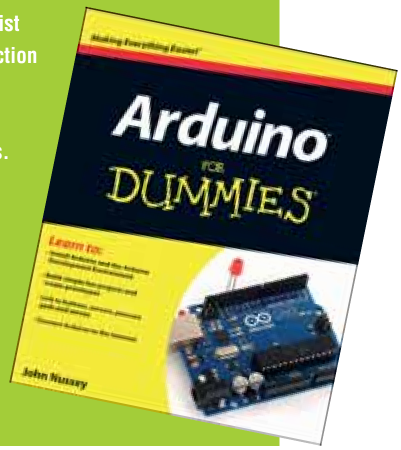


```
if (brightness == 0 || brightness == 255) {
fadeAmount = -fadeAmount ;
}
// wait for 30 milliseconds to see the dimming effect
delay(30);
}
```

Upload this sketch to the board, and if everything has uploaded successfully, the LED fades from off to full brightness and then back off again. If you don't see any fading, double-check the wiring:

- Make sure the correct pin numbers are being used.
- Check the LED is correctly positioned, with its long leg connected by a wire to pin 9 and the short leg connected via the resistor and a wire to GND.
- Check the connections on the breadboard. If the jumper wires or components are not connected using the correct rows in the breadboard, they will not work. ●

More on this and other Arduino projects can be found in the 'Arduino For Dummies' book by John Nussey.

Digital CMOS Circuits

MAURIZIO DI PAOLO EMILIO, PHD IN PHYSICS AND A TELECOMMUNICATIONS ENGINEER, PRESENTS THIS SERIES OF ARTICLES ON THE FUNDAMENTALS OF MICROELECTRONICS

It is virtually impossible to find electronic devices in our daily lives that do not contain digital circuits, most of them with CMOS logic at their heart.

There are a large number of CMOS devices, in a number of families. Using very few components it is possible to build fairly elaborate pulse and signal generators.

CMOS Logic

Depending on the doping material used, there are mainly two types of metal-oxide-semiconductor field-effect transistors (MOSFETs) – the n-channel, or nMOS, and p-channel, or pMOS. In N-type metal-oxide-semiconductor (NMOS) logic, n-type MOSFETs are used to implement logic gates and other digital circuits. These circuits are mostly used for switching due to their high-speed nature, whereas PMOS circuits are slow to transition from high to low state, and their asymmetric input logic levels makes them susceptible to noise (Figure 1).

However, complementary metal-oxide-semiconductor (CMOS) technology offers some attractive practical advantages over NMOS technology: high noise-immunity and low static-power consumption. CMOS uses a combination of p- and n-channel MOSFETs as building blocks, but here both low-to-high and high-to-low output transitions are fast since the pull-up transistors have low resistance when switched on, unlike the load resistors in NMOS logic. In addition, the output signal swings the full voltage between the low and high rails. This strong, nearly symmetric response also makes CMOS more resistant to noise.

In NMOS circuits the logic functions are realized by arrangements of NMOS transistors, combined with a pull-up device that acts as a resistor. The concept of CMOS circuits is based on replacing the pull-up device with a pull-up network (PUN) that is built using PMOS transistors, such that the functions realized by the PDN and PUN networks are complements of each other. Then a logic circuit, such as a typical logic gate, can be implemented as shown in Figure 2.

The generic pattern of a CMOS gate that implements a more complex logic function is shown in Figure 1. It comprises a network of NMOS transistors (pull-down network) and a network of PMOS transistors (pull-up network), each consisting of an equal number of transistors. Each input variable requires an NMOS transistor in the pull-down network and a PMOS transistor in the pull-up network.

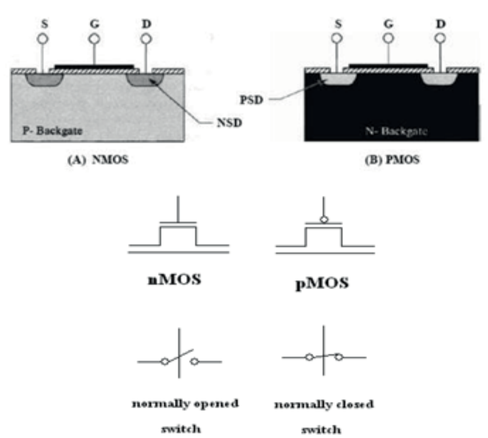

Figure 1: NMOS and PMOS structures

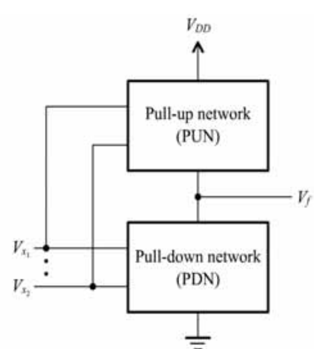

Figure 2: The structure of a CMOS circuit

CMOS Inverter

A CMOS inverter (Figure 3) is composed of two MOSFETs, with their gates connected to the inverters' input line, and their drains to the output line.

The input resistance of the CMOS inverter is extremely high, as the gate of an MOS transistor is virtually a perfect insulator and draws no input direct current. Since the input node of the inverter only connects to the transistor gates, the steady-state input current is nearly zero.

A single inverter can theoretically drive an infinite number of gates (or have an infinite fan-out).

A CMOS inverter dissipates a negligible

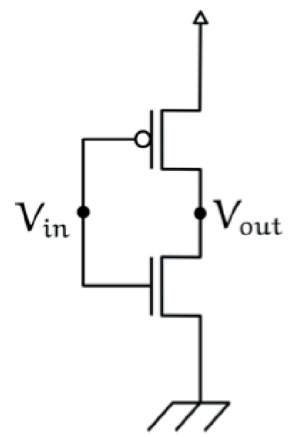

Figure 3: CMOS inverter

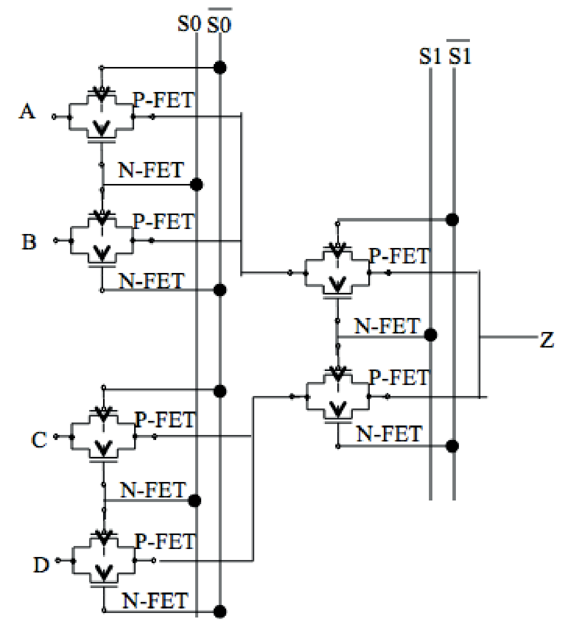

Figure 4: Multiplexer

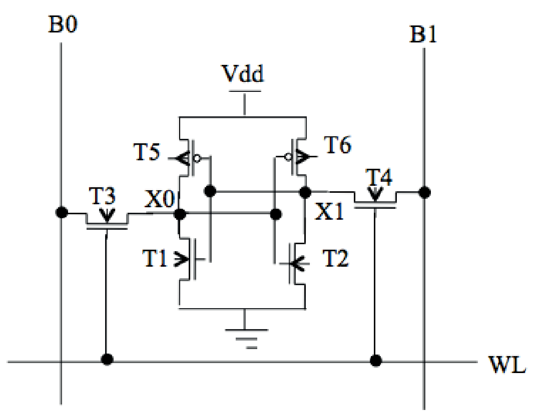

Figure 5: SRAM cell

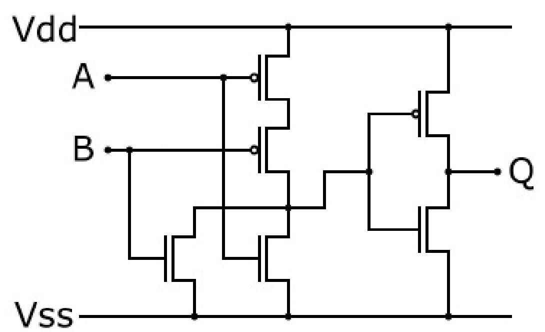

Figure 6: CMOS OR

amount of power when operating in steady state, which occurs only during switching. This makes CMOS technology usable in low power and high-density applications.

Some Simple Circuits

Multiplexer:

Multiplexers (Figure 4) can be implemented with standard CMOS logic gates, CMOS transmission gates or a combination of both. With CMOS gates, a 2-to-1 multiplexer requires three gates: two ANDs and one OR.

A CMOS transmission gate can be constructed as a parallel combination of NMOS and PMOS transistors, with complementary gate signals. The main advantage of the CMOS transmission gate over an NMOS one is it allows the input signal to be transmitted to the output without any threshold voltage attenuation.

SRAM Cell:

Static random access memory (SRAM) can retain its stored information as long as power is supplied. Its circuit schematic is shown in Figure 5. It comprises two cross-coupled inverters (positive feedback), in particular four n-FETs and two p-FETs. The core of the cell is formed by two CMOS inverters, where the output potential of each inverter is fed as input to the other. This feedback loop stabilizes the inverters to their respective states.

Access to the cell is enabled by the word line (WL); moreover, bit lines (indicated with B0-B1) are used to read and write from, and to, the cell.

CMOS OR:

The OR gate (Figure 6) is a digital logic gate that implements a logical disjunction: a HIGH output results if one or both inputs to the gate are HIGH. OR gates are basic logic gates and, as such, they are available in TTL (transistor-transistor logic) and CMOS ICs logic families. TTL is a class of digital circuit built from bipolar junction transistors (BJTs) and resistors. TTL became the foundation of computers and other digital electronics.

IAN DARNEY PRESENTS A SERIES OF ARTICLES ON CIRCUIT MODELLING FOR ELECTROMAGNETIC COMPATIBILITY

Bench Testing

This is the fourth article in the series '*Circuit Modelling for Electromagnetic Compatibility*'. The first three articles have described a systematic method of deriving circuit models from the relationships of Electromagnetic Theory. These models can be used to simulate interference coupling mechanisms and can be analysed using the much simpler mathematics of Circuit Theory. However, there comes a point when pure theory is not enough and practical tests are necessary. Such tests can be carried out by using a signal generator, an oscilloscope and a couple of transformers assembled from readily available electronic components.

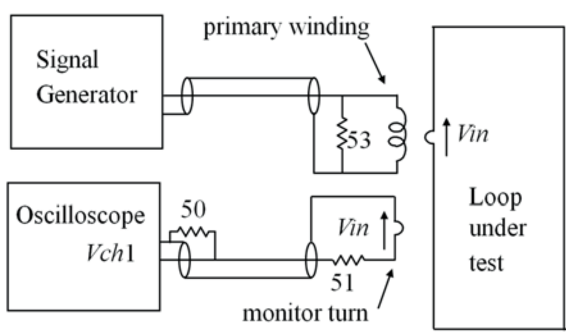

Figure 1: Use of voltage transformer

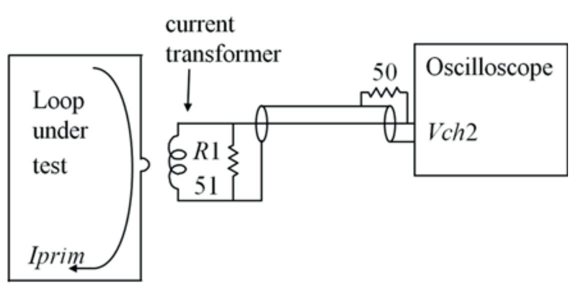

Figure 2: Use of current transformer

Voltage Transformer

The voltage transformer is essentially a clamp-on ferrite core with a primary winding of ten turns and a single-turn monitor winding, configured as shown in Figure 1.

The core is clamped around the conductor or cable of the loop-under-test and a sinusoidal signal applied to the primary. The 53-ohm resistor ensures that the output voltage of the primary winding is reasonably constant over the operating bandwidth. The ten-to-one turns ratio ensures that the impedance reflected into the loop-under-test is very low: about 0.25 ohms. The monitor turn allows the actual voltage injected into the load to be measured. The 50-ohm resistor at the oscilloscope input makes the co-axial cable transparent.

Current Transformer

The ferrite core of this transformer is identical to that of the voltage transformer, but this time it is the secondary which has ten turns (see Figure 2). Current delivered to the secondary is one-tenth that in the loop-under-test.

A current source in parallel with a resistor is equivalent to a voltage source in series with that resistor. So the output impedance of the secondary is matched to the characteristic impedance of the co-axial cable.

Figure 3 shows the circuit model of the current transformer assembly. This was created by subjecting the unit to a calibration test, where the input current was independently monitored and the output voltage *Vch2* was measured by the oscilloscope. The red circles in Figure 4 show the frequency response of the transfer impedance *ZTt* derived from the test results, where:

$$ZTt = \frac{Vch2}{Iprim} \tag{1}$$

The blue curve, *ZTm*, was obtained by analysing the response of the model. Initially, the two curves were quite separate. By adjusting component values in the model, the blue curve could be moved closer to the red circles. The inductance *L1* was determined by co-locating the rising edges; *R1* by co-locating the flat portions between 100kHz and 2MHz, and *C1* and *R4* by co-locating the flat regions between 2MHz and 20MHz.

Having achieved close correlation between the two curves, it became possible to use the model to calculate the amplitude of the current in the loop-under-test, given data on frequency and the peak-to-peak amplitude of *Vch2*.

Co-axial Cables

A basic requirement for any test setup which measures interference coupling is that the test equipment should not itself cause interference. Since any such setup involves the routing of co-axial cables in close proximity to each other, it is essential that cross-coupling between these cables be kept to an absolute minimum. One way of doing this is to add an outer screen to each cable, as shown by Figure 5. This can be done by removing the insulation from the shells of the co-axial connectors, slipping a screen braid over the cable and making off the ends of this outer braid to the connector shells. An insulating braid can then be used to cover the screen braid.

> "There comes a point when pure theory is not enough and practical tests are necessary

The Isolated Conductor

The simplest wiring configuration which can be envisaged is the isolated conductor.

Figure 6 illustrates a setup used to measure the characteristics of a 15m length of 14/0.2 equipment wire. The voltage transformer injects a sinusoidal voltage *Vtest* into the centre section of the conductor; channel 1 of the oscilloscope monitors this voltage and channel 2 monitors the output current *Itest*. The red circles in Figure 7 display the measured response of the admittance *Yt*, where:

$$Yt = \frac{Itest}{Vtest} \qquad (2)$$

A circuit model of this assembly was constructed, using the techniques described in the article on *'Transmission Lines And Antennae'* (see model in Figure 8). The inductance of each monopole was calculated using:

$$Lp = \frac{\mu_o \cdot \mu_r \cdot l}{2 \cdot \pi} \cdot \ln\left(\frac{l}{r}\right) = 14.42 \text{ micro-H} \qquad (3)$$

where l = 7.5m and r = 0.5mm.

The frequency *fq* at which maximum current was observed

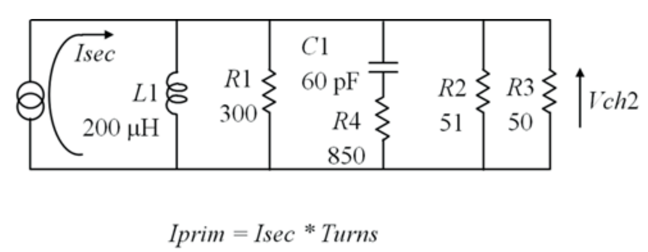

Figure 3: Representative curcuit model of current transformer

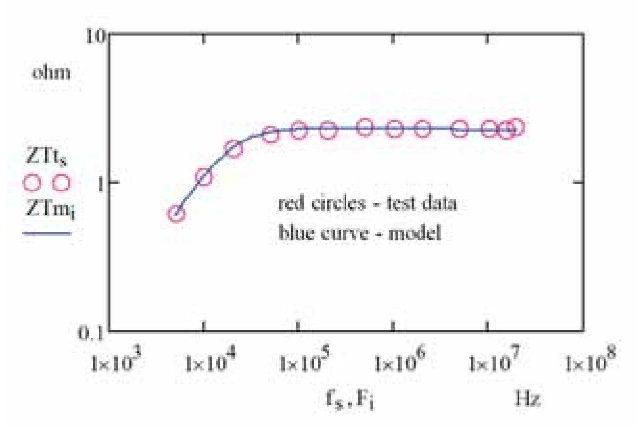

Figure 4: Transfer impedance of current transformer

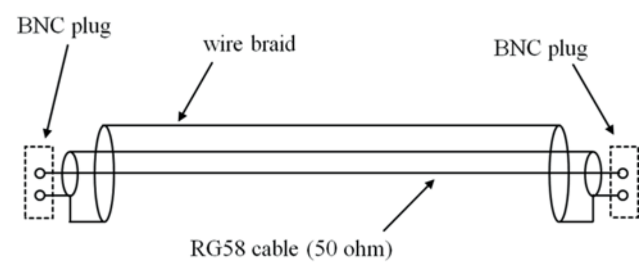

Figure 5: Tri-axial cable

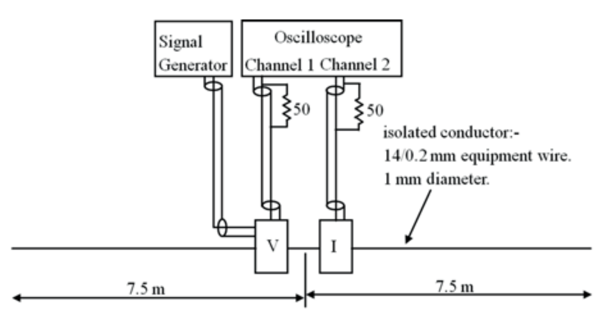

Figure 6: Testing the response of an isolated conductor

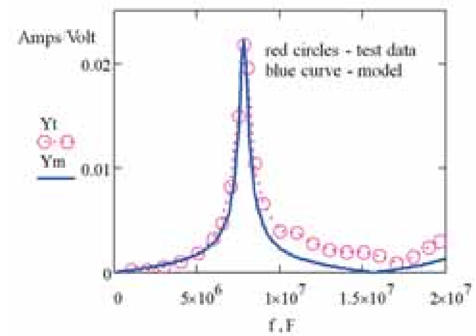

Figure 7: Response of an isolated conductor

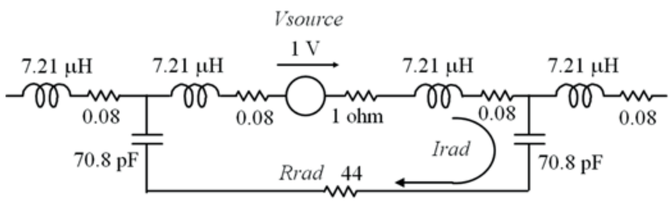

Figure 8: Curcuit model of an isolated conductor acting as a dipole

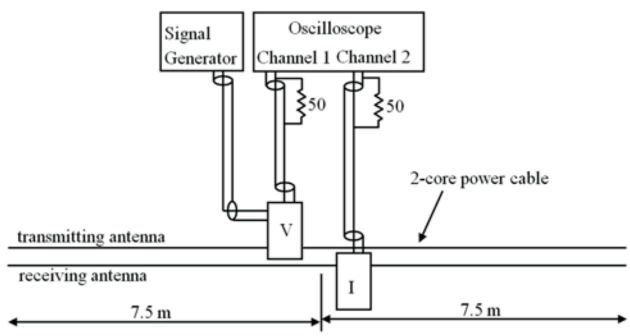

Figure 9: Test to measure transmission line characteristics of cable

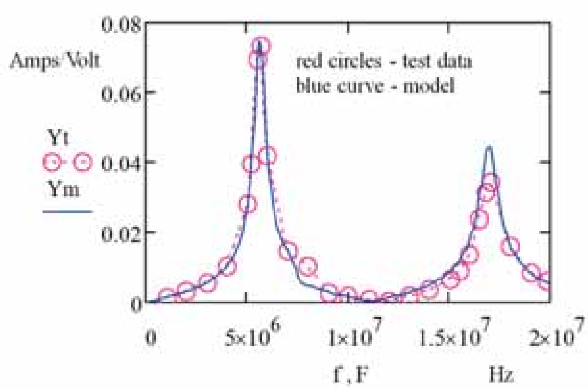

Figure 10: Coupling between two adjacent conductors

was 7.83MHz. This datum allowed the propagation velocity v to be calculated:

$$v = 4 \cdot l \cdot fq = 2.439 \cdot 10^8 \quad \text{m/s} \tag{4}$$

The relative permittivity of the insulation was then derived:

$$\varepsilon_r = \left(\frac{c}{v}\right)^2 = 1.631 \tag{5}$$

where c = 300Mm/s.

The capacitance of each monopole was given by:

$$Cp = \frac{2 \cdot \pi \cdot \varepsilon_o \cdot \varepsilon_r \cdot l}{\ln\left(\frac{l}{r}\right)} = 70.77 \text{ pF} \tag{6}$$

The admittance of the circuit of Figure 8 is:

$$Ym = \frac{Irad}{Vsource} \tag{7}$$

Using the process described in the article on transmission lines and antennae, a Mathcad program was then compiled to calculate the value of the admittance *Ym* over the same range of frequencies as measured by the test equipment. This gave a curve similar to that of the test results. However, the amplitude of the peak was lower than that derived from test data, due to the selection of the textbook value of 73 ohm for the radiation resistor. Decreasing the value of *Rrad* to 44 ohms gave the solid blue curve of Figure 7.

Since the response of the model replicates that of the test results, Figure 8 can be regarded as a representative circuit model which defines the characteristics of the conductor-under-test. Effectively, the test results were used to measure the values of the radiation resistance and the propagation velocity.

So a significant conclusion from this particular test is that it is possible to measure the amplitude and velocity of antenna current using general-purpose test equipment.

Photons

It is clear from the test results that when a voltage of 1V at 7.83MHz is induced into the conductor, a current of 22mA flows in the centre section. The theory of antennae shows that as it propagates along the conductor, its amplitude decreases. At each end, the current has decayed to zero. The energy lost to the conductor has morphed into that of an electromagnetic wave which radiates out into the environment. The two monopoles radiate energy of different polarities.

The model of Figure 8 depicts this interchange as a current which flows out of one monopole, through the radiation resistance and back via the other monopole.

Since current flows along the conductor at a velocity comparable with the speed of light, it cannot be carried by electrons. The carrier must be sub-atomic particles, or photons. The Wikipedia definition is '*A photon is an elementary particle, the quantum of light and all other forms of electromagnetic radiation*.'

The conclusion must be that 'current' is a measure of the flow of photons and that it flows out radially from a conductor, as well as along the conductor.

Cable Characterisation

The setup of Figure 9 illustrates a very similar test, carried out on a twin-conductor cable. This time, the voltage source was used to inject a voltage in one conductor, whilst the current transformer was used to monitor the current in the other. Since both ends of the cable were left open circuit, the configuration can be likened to a dipole transmitting antenna laid alongside a receiving antenna. Current flows out via the transmitter and back via the receiver.

The setup can also be viewed as two open-circuit transmission lines connected back-to-back. The circles on Figure 10 are essentially measurements of the differential-mode current at a set of spot frequencies, when the source voltage is held at 1V. The quarter-wave frequency of each 7.5m line is 5.7MHz, indicating that the differential-mode current has a propagation velocity of about 170Mm/s.

The second peak at 16.5MHz is due to resonance at a frequency corresponding to three-quarters of a wavelength.

Figure 11 illustrates the setup when the current transformer was clamped around both conductors. This time the measurements were of the antenna-mode current (see the circles in Figure 12). The most notable observation was that the frequency of the peak was 7.4MHz, which was significantly higher than that of the frequency of the peak differential-mode current.

This means that antenna current travels at a higher velocity than differential-mode current. These currents must be separate entities, separate but interdependent.

Figure 13 is a circuit model which simulates the coupling mechanisms. This model was constructed using the technique described in the article '*Transmission lines and antennae*' and provides a possible clue to the reason for the different velocities. Current flowing along the transmitting conductor creates an electromagnetic field. This field then links with the receiving conductor and creates a current flow in the opposite direction – a process that takes time. Differential-mode current must lag behind aerial-mode current.

Details of this series of tests can be found in Chapter 7 of my book '*Circuit Modeling for Electromagnetic Compatibility*'. ●

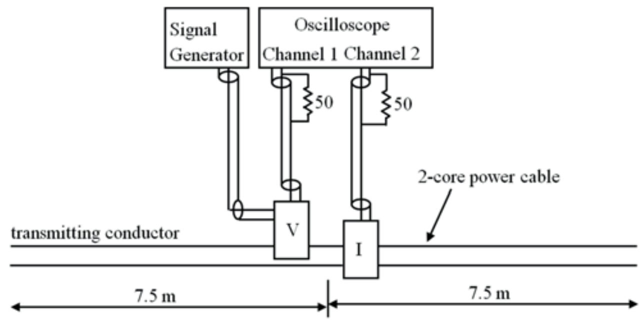

Figure 11: Test to measure emitted radiation characteristics of cable

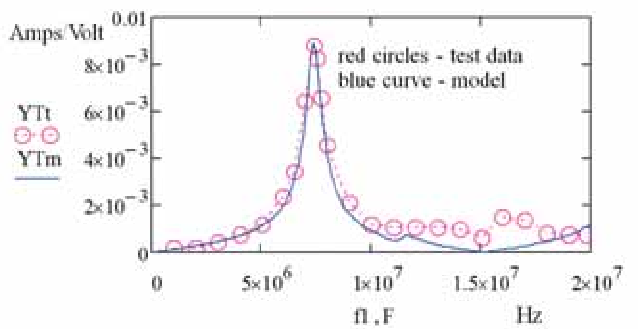

Figure 12: Radiated emission of cable

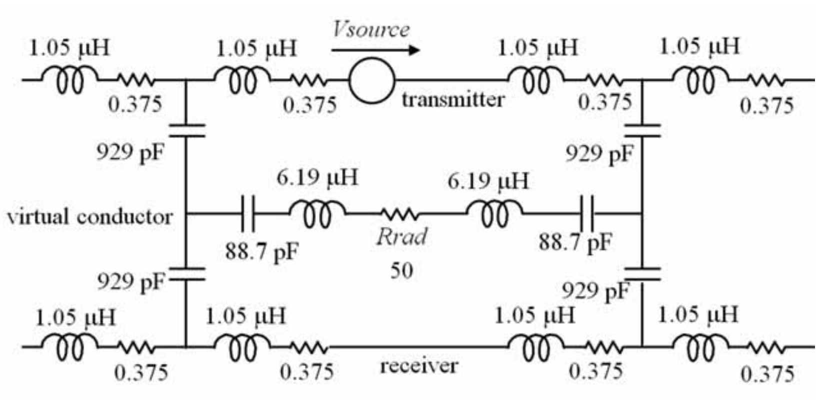

Figure 13: Representative circuit model of cable under test

PCIM

20-22nd May, Nuremberg, Germany

www.pcim-europe.com

PCIM
EUROPE

International Exhibition and Conference for Power Electronics, Intelligent Motion, Renewable Energy and Energy Management
Nuremberg, 20 – 22 May 2014

PCIM Europe 2014 Continues To Grow

About 400 companies are expected to exhibit at this year's PCIM Europe in Nuremberg (20 – 22 May), reflecting the growing importance of the world's leading meeting point for the power electronics sector. In three halls and over an area of approximately 20,000 square meters, key companies in the sector will showcase their products and services to an international trade audience. The additional exhibition hall will provide visitors with a concentrated overview of the market.

Highly specialised project presentations, expert discussions and market overviews will be delivered by companies, trade associations and the trade press at the Industry Forum in Hall 6. The Exhibitor Forum in Hall 9 will also offer more than 50 vendor presentations from exhibiting companies on their latest developments and innovations.

This year's focus is on the latest trends in power electronics components and systems for use in the wind and solar energy sector. The exhibition and conference have a role to play together in the ambitious project to significantly increase the proportion of renewable energies for generating electricity.

Along with products and solutions on display at the exhibition, visitors will be able to attend vendor presentations and contribute to expert discussions on the latest developments in wind and solar energy at the free industry forums. For example, Infineon Technologies will tackle the topic "*Power Semiconductors in Energy Efficient Smart-Grid Installations*".

Visitors will also learn what technological challenges such as energy harvesting, long-distance energy transfer and efficient energy consumption represent for the industry.

Conference Offers Feature Session

With over 250 presentations on new technological trends in power electronics components and systems, the conference program offers a comprehensive overview of the latest power electronics topics.

A highlight at the beginning of each day of the conference are the the keynote speeches: "*Progress in Power Semiconductor Devices and Applications*", delivered by Dan Kinzer of Fairchild Semiconductors; "*Ultra High Voltage SiC Power Devices and Its Impact on Future Power Delivery System*" by Alex Huang of NSF FREEDM Systems Centre; and "*E-Mobility 2020: Power Electronics, a Key Technology for the Effective Deployment of Electric Vehicles in a Low Carbon Society*" by Enrique J. Dede of ETSE University Valencia.

In addition to the these speeches, there are six seminars and ten tutorials. In a feature session entitled "*New and Renewable Energy Systems*" experts will report on the development of a hybrid power generation system that could provide an independent and environmentally-friendly energy supply to residential areas.

The session "*A Low Cost Photovoltaic Maximum Power Point Tracking Buck Converter for Remote Cell Phone Charging Applications*" looks at how photovoltaic hybrid systems can be used to centrally generate the total energy supply for remote areas from renewable energies.

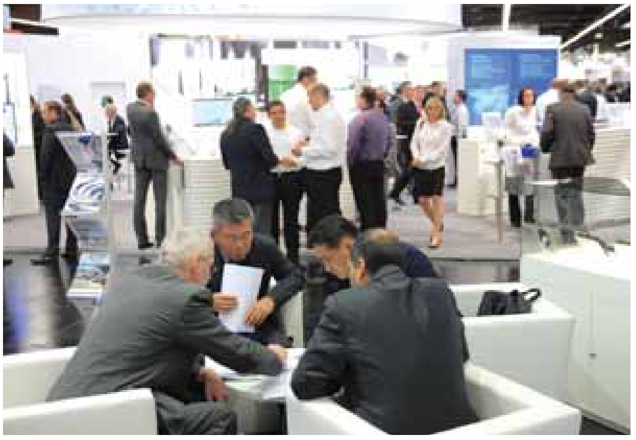

On Tuesday 20th of May, the European power electronic research network ECPE and EU Projects, which support the idea of "*European Power Electronics Leadership*", will introduce themselves at the industry forum in Hall 6.

As part of Horizon 2020, the EU provides 4.8bn Euros of appropriation, part of which is being used to develop a leading European role in power electronics. Simona Rucareanu or ENIAC JU will give a program overview and present the funding opportunities for power electronics in Europe.

On Wednesday 21st of May, current topics such as the advantages of Silicon over Siliconcarbide (SiC) and Gallium Nitride (GaN) technologies in inverter and energy supply applications will be debated. Representatives of ABB, Cree, EPC, Infineon, International Rectifier, Mitsubishi, Semikron, ST Microelectronics, Toshiba and Transphorm will participate in this panel discussion round.

Seminars And Tutorials Delivered By Experts

On the two days before the conference gets underway, internationally renowned experts will share their knowledge of power electronics in six half-day seminars and 10 full-day tutorials. For the first time, the program will include a tutorial on "*Power Electronics and Control for Grid Integration of Renewable Energies and Energy Storage Systems*". This tutorial serves the growing demand for training in power electronics and solutions for renewable energies.

On all days of the exhibition, over 50 exhibitors will each present their newest developments, innovations and solutions in 20-minute presentations in Hall 9. Vishay, Thales Microelectronics, Indium, Mentor Graphics, Vincotech, Magnetec, Fairchild, Rohm Semiconductor, Yokogawa, Alpha, Heraeus, Powersem, Analog Devices and Hitachi are just a few of the companies informing forum visitors of their product highlights.

For a detailed conference program and an up-to-date list of exhibitors participating at the PCIM exhibition go on line at ***www.pcim-europe.com***

LOW-PROFILE, HIGH-POWER RESISTORS USE THICK-FILM TECHNOLOGY

UK-based Arcol Resistors now offers its TFBR series of high power-density, low-profile, thick-film technology high-power resistors. Designed for easy assembly and supplied with a variety of terminal styles, the leading-edge thick-film technology low-inductance design lends itself to high frequency operation due to its low inductance characteristics. The added benefit of high instantaneous pulse capacity (Energy = 120J for pulses ≤ 1s and cycle 2s) also makes the TFBR suitable for braking, snubbing and discharge requirements.

The TFBR series incorporates an innovative packaging design, providing a high power density in a very low-profile package. The substrate thickness is a tiny 1.0 ± 0.2mm and the power dissipation (on a heat sink) is 100W for the TFBR100, 300W for the TFBR300 and 900W for the TFBR900. Ohmic values are available over the range 5R to 680R.

The other main characteristics include a tolerance of ±10% standard and an operating temperature is -55°C to +200°C.

www.arcolresistors.com

ULTRA MINIATURE OCXO DELIVERS ±5PPB STABILITY IN A SMALL PACKAGE

In an industry standard package measuring just 14 x 9.0mm and with a height of only 6.5mm, IQD's new IQOV-162 series OCXO provides a frequency stability down to ±5ppb (parts per billion) over the full industrial temperature range from -40 to 85 degrees C.

In addition to this exceptional size/performance ratio, the new model is available in a very wide frequency range: from 10 to 100MHz. Operating from a 3.3V supply voltage, the IQOV-162 consumes 600mA of current during warm-up and takes less than five minutes to be within < 100ppb of the final specification and 300mA max at steady state @25 degrees C.

The output can be specified as either HCMOS, 15pF load or sinewave, into a 50 Ohms load. As well as offering phase noise performance better than -150dBc/Hz @ 1kHz offset, ageing performance is also extremely good at less than ±500ppb per year.

www.iqdfrequencyproducts.com

4KB SERIAL PRESENCE DETECT EEPROM FOR DDR4 SDRAM MODULES

Microchip announces a new 4Kb I2C Serial Presence Detect (SPD) EEPROM: the 34AA04. This device is specifically designed to work with the next generation of Double Data Rate 4 (DDR4) SDRAM modules used in high-speed PCs and laptops, while also supporting older DDR2/3 platforms.

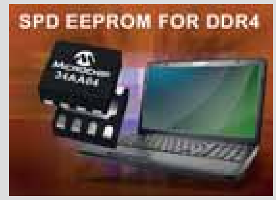

This new EEPROM is designed for the price-competitive consumer products market and is capable of operation across a broad voltage range of 1.7V to 3.6V. The 34AA04 is JEDEC JC42.4 (EE1004-v) Serial Presence Detect (SPD) compliant and is designed to be compatible with DDR4 SDRAM modules. The 34AA04 includes reversible software write protection for each of four independent 128 x 8-bit blocks and supports a new SMBus-compatible bus time-out. The device also features a page-write capability of up to 16 bytes of data and three address pins allow up to eight devices on the same bus.

The 34AA04 is backward compatible with existing DDR2 and DDR3 SPD EEPROMs.

www.microchip.com/get/CKQL

ULTRACMOS RF POWER LIMITERS: INDUSTRY'S FIRST MONOLITHIC ALTERNATIVE TO DISCRETE, PIN-DIODE LIMITERS

Peregrine Semiconductor debuts a new line of UltraCMOS RF power limiters, including PE45140 and PE45450 slated for release in May. Peregrine's power limiters represent the industry's first turnkey, monolithic solutions to provide an alternative to discrete, PIN-diode limiters based on gallium arsenide (GaAs). UltraCMOS power limiters deliver simple, repeatable and reliable protection ideal for test and measurement, land mobile radio (LMR), wireless infrastructure, military and radar systems.

On a chip eight times smaller than the board space required by discrete, PIN-diode solutions, Peregrine's new power limiters provide a 10-100X improvement in response and recovery time; and deliver greater than 40dB improvement in linearity (IP3) and offer a 20X improvement in ESD (electrostatic discharge) protection.

Of particular interest to RF designers, Peregrine's power limiters save PCB space with a small form-factor; reduce BoM (bill of materials) by eliminating the need for extra components; and improve time to market by reducing in-design time and costs.

www.psemi.com

SENSIRION'S LIQUID FLOW SENSOR FLIES INTO SPACE

On May 6, a rocket will lift off bound for the International Space Station (ISS). On board will be a liquid flow sensor from Sensirion AG, Stäfa, Switzerland. The sensor is part of a research project by Minnehaha Academy in Minnesota that is investigating the impact of microgravity on the effectiveness of liquid flow. Among other potential findings, the project aims to shed light on the effects of weightlessness on the circulatory system.

The LS16 liquid flow sensor from Sensirion on board the ISS will measure the flow of demineralized water generated by a piezoelectric pump in zero gravity, and compare the results with those of a control experiment on earth. Numerous applications in fluid dynamics, physics, biology and hemodynamics (the forces involved in the circulation of blood) will benefit from these findings.

To ensure that the sensor could withstand the enormous forces during lift-off, Sensirion's development team replaced the capillary glass tubes with robust capillary steel tubes.

www.sensirion.com

MICROCHIP INTRODUCES COST-EFFECTIVE 8-BIT PIC MICROCONTROLLER FAMILY

Microchip announces, from EE Live! and the Embedded Systems Conference in San Jose, the PIC16(L)F170X and PIC16(L)F171X family of 8-bit microcontrollers (MCUs), which combines a rich set of intelligent analogue and core independent peripherals, with cost-effective pricing and eXtreme Low Power (XLP) technology. Available in 14-, 20-, 28- and 40/44-pin packages, the 11-member PIC16F170X/171X family of MCUs integrates two op-amps to drive analogue control loops, sensor amplification and basic signal conditioning, whilst reducing system cost and board space. These new devices also offer built-in Zero Cross Detect (ZCD) to simplify TRIAC control and minimise the EMI caused by switching transients. Additionally, these are the first PIC16 MCUs with Peripheral Pin Select, a pin-mapping feature that gives designers the flexibility to designate the pin-out of many peripheral functions.

The PIC16F170X/171X are general-purpose MCUs that are ideal for a broad range of applications, from consumer home appliances to power tools and portable medical products among others.

www.microchip.com

NEXT-GEN EVOLUTION OF FFLC SERIES FILM CAPACITORS

AVX has evolved its FFLC Series medium power film capacitors for DC filtering applications. Available in large case sizes up to 35 liters, the new FFLC Series capacitors exhibit higher specific energy than equivalent solutions (up to 240J/l) and feature AVX's controlled self-healing technology, which enables safe, high reliability, long lifetime performance with no risk of explosion.

Also available with a low stray inductance option that enables high frequency ripple current, the series is ideal for DC filtering in any variety of power conversion applications, and is particularly well-suited for applications that require enhanced safety and reliability, including rail applications, such as main or auxiliary inverters; new energy applications, such as wind turbines and solar PV inverters; and industrial applications, such as motor drives.

Comprising metallized, segmented polypropylene film encased in unpainted, rectangular, resin-filled aluminum cases, FFLC Series capacitors feature two mounting brackets and either four M8/15 female connections or four M12/30 male connections.

www.avx.com

TE CONNECTIVITY FORMS STRATEGIC ENGAGEMENT WITH TTI EUROPE

TE Connectivity (TE) has entered into a strategic partnership with TTI Europe, a specialist distributor of passive, connector, electromechanical and discrete components. The engagement is part of the TE Industrial business unit strategy to provide customers with improved service levels and an exceptional customer experience, while extending the geographic reach of its products.

As a result of the new partnership, TE's Industrial business unit will achieve greater coverage and focus in the EMEA market, with customers now able to leverage TTI's broad and deep stock and design-in support of TE Industrial products. Additionally, customers will benefit from extensive pre-provisioned inventory with low Minimum Order Quantity (MOQ) conditions on select product programs. The engagement launches with a specific focus on TE heavy duty connectors. Further, TE has invested more to expand its field-based technical expertise, and when combined with TTI's global industry-leading stock management solutions, customers will experience additional benefits.

www.ttieurope.com

POWER INTEGRATIONS ANNOUNCES 'ULTIMATE IN STANDBY PERFORMANCE'

Power Integrations announced a new reference design for an 8W, universal-input auxiliary power supply that achieves zero standby power consumption for appliance applications. Based on a member of Power Integrations's LinkZero-LP family of ICs, DER-417 is a universal-input, 5V, 1600mA flyback power supply that consumes less than 4mW at 230VAC and provides 1mW of power in standby mode.

Products such as TVs, appliances, security and monitoring systems, and HVAC equipment use power while waiting to be used or while monitoring sensor inputs prior to executing their proper functions. This wasted power amounts to both an environmental cost and an economic cost to households and businesses. Lawrence Berkeley National Laboratory has estimated that standby power accounts for 5-10% of residential electricity use in the developed countries, and is responsible for approximately 400 million tons of global CO2 emissions each year.

www.powerint.com

VERY LOW ON-RESISTANCE LOAD SWITCH WITH CONTROLLED TURN-ON

Advanced Power Electronics Corp (USA) has recently launched a small load switch with controlled turn-on and very low on-resistance.

The APE8937-HF-3 load switch contains one N-channel MOSFET that can operate over a wide input voltage range from 0.8V to 5.5V and support a maximum continuous current of up to 4A.
The on-resistance is very low with only 22mΩ from VIN = 1.8V to VIN = 5.0V. The switch is controlled by an on/off input and is capable of interfacing directly with control signals as low as 0.8V.

Additional features include a 300Ω on-chip load resistor for output quick discharge when the switch is turned off. For power sequencing, the rise time is adjustable by an external ceramic capacitor on the CT pin, which also reduces inrush current.

The APE8937-HF-3 switch is available in an ultra-small, space-saving 2mm x 2mm 8-pin DFN package with thermal pad.

www.a-powerusa.com

THE ATMEL SAMA5D3 XPLAINED EVAL KIT IS NOW AVAILABLE FROM MOUSER

Mouser Electronics is now stocking and shipping the Atmel SAMA5D3 Xplained Evaluation Kit, a low-cost prototyping board for the Atmel SAMA5D3 family of processors based on the ARM Cortex A5 processor core. The board supports an external LCD interface, Gigabit Ethernet and Arduino R3 expansion headers.

The Atmel SAMA5D3 Xplained Evaluation Kit available from Mouser Electronics is Atmel's latest in a series of SAMA5D3 evaluation boards. This SAMA5D3 Xplained kit allows developers to easily evaluate the high level features of the SAMA5D3 processor. The board comes with 256Mbytes DDR2 DRAM, 256Mbytes NAND Flash, and has an SD card connector and a microSD slot. An LCD interface connector is supported by an LCD TFT controller with touchscreen capabilities.

Two Ethernet connectors are available, one for 10/100 and the other for Gigabit Ethernet. There are two USB host ports as well as one micro AB USB connector.

www.mouser.com

HARWIN INVESTS £500K IN THE UK

Harwin has taken delivery of equipment worth £500,000 at its Portsmouth manufacturing headquarters, facilitating further production efficiencies and enabling the company to remain competitive.

Maintaining a vertically-integrated manufacturing capability in the UK is a firm commitment that underpins Harwin's entire business strategy. The new investment with automatic stamping press maker, Bruderer, sees Harwin achieve a world first with the integration of a planetary gearbox into the shaft of the main stamping press motor. This means that Harwin can use the same equipment for development and production, identifying any issues at the lowest stroke rate before flicking a switch to move to full production rates. This is particularly beneficial for the development of Harwin's EZ-Boardware range of surface mount products that improve manufacturing flexibility, reduce manufacturing costs and improve in-field maintenance.

Traditional methods used to solve cable management, test and EMC problems and battery retention often require secondary, manual processing.

Damon de Laszlo (left), Chairman of Harwin plc, and Andreas Fischer, CEO of Bruderer

www.harwin.co.uk

SIGNS OF SUCCESS: LED DISPLAY KEEPS TABS ON VOLVO OCEAN RACE

Press visitors to the Media Centre at the Volvo Ocean Race benefit from continuous updates via RSS feed relayed to an LED display system supplied by Messagemaker Displays. The display, which involves complex routings and turns, runs around most of the perimeter of the print centre, making it attention grabbing and a truly unique display.

The Volvo Ocean Race (formerly the Whitbread Round the World Race) is a circumnavigational race, held every three years. Commencing this autumn at Alicante in Spain, the latest race will conclude in Gothenburg in Sweden during early 2015. During the race, teams will cover over 70,000km (40,000 nautical miles) of the world's seas and is the ultimate test of sailing skills and physical endurance.

Messagemaker supplied an LED solution to exacting bespoke requirements via Electrosonic, a global audio-visual company with extensive experience in designing and supplying complex systems incorporating state-of-the-art technology for the professional AV market.

www.messagemaker.co.uk

OPTICAL SPECTRUM ANALYSER INCORPORATES NEW FUNCTIONS

The new Yokogawa AQ6370D benchtop optical spectrum analyser is a successor to the company's best-selling AQ6370C and incorporates a number of new functions designed to enhance its accuracy and analysis capabilities in the 600-1700nm wavelength range. Newly added functions include data logging, gate sampling, resolution calibration, an advanced marker function and an enhanced auto-sweep mode.

The data logging function records analysis results such as WDM analysis (OSNR, optical signal/noise ratio), distributed feedback laser diode (DFB-LD) analysis and multi-peak measurements at up to 10,000 points per channel with time stamps. Recorded data can be displayed in a table and graphical format. This function is useful for the long-term stability testing and temperature cycle testing of systems and devices. The optical spectrum of each measurement can also be stored for reviewing and troubleshooting.

The advanced marker function adds markers to obtain the power density and the integrated power of a designated spectrum.

www.tmi.yokogawa.com

HIGH-CURRENT SYNCHRONOUS BUCK REGULATOR OFFERS HIGH EFFICIENCY

The new A8672 from Allegro MicroSystems Europe is a synchronous buck regulator IC capable of delivering high currents (up to 8A) through the use of low on-resistance internal switches. It uses valley current mode control, which allows very short 'on' times to be achieved and inherently provides improved transient response over traditional switching schemes through the use of a voltage feed-forward loop and frequency modulation during large signal load changes.

The A8672 includes a comprehensive set of diagnostic flags, allowing the host platform to react to a myriad of different fault conditions. A fault output indicates when either the temperature is becoming unusually high, or a single point failure has occurred – such as the switching node shorted to ground or the timing resistor going open-circuit. A "power OK" output is also provided after a fixed delay to indicate when the output voltage is within regulation.

www.allegromicro.com

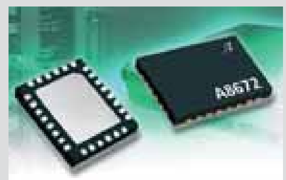

INTELLICONNECT CONNECTOR SOLUTIONS FOR MEDICAL ELECTRONICS SYSTEMS

Intelliconnect (Europe) Ltd offers a wide range of connectors suitable for use in diagnostic, treatment and wearable medical device technologies, including connectors for RF cancer treatment, radiation dosimeters and detectors, bio-medical test equipment and bionics.

Intelliconnect also manufacture micro-miniature waterproof coaxial connectors for use in cochlear ear implants. This very demanding application requires a rugged and reliable quick-disconnect waterproof connector capable of making several thousand disconnects during its product lifetime. The design meets IP68, is comfortable to wear close to the skin and may be used in normal domestic environments including swimming pools, showers, baths and high humidity environments such as saunas, steam rooms etc.

In addition to standard coaxial and triaxial types, Intelliconnect provide a fast turnaround custom design service for non-standard medical connector requirements. With no NRE costs to customers and low minimum order quantities, Intelliconnect custom designed medical connectors offer an ideal solution for specialised medical products.

www.intelliconnect.co.uk

HARTING EXPANDS PRELINK CONNECTOR FAMILY

Harting has expanded its connector family based on Ha-VIS preLink technology by adding a robust universal M12 connector housing designed to incorporate a range of connector modules.

New modules that can be used in the M12 housing include a D-coded version for 4-core data cables with transfer rates of up to 100Mbit/s or a variant with X-coding for 8-core data cables, suitable for applications at up to 10Gbit/s.

Among the special features of Harting's preLink connection technology is a terminal block connected to the individual cores of the data cable via internal insulation displacement terminations which remain stable over time and are vibration-proof. The cable assembled in this way is attached securely to the connector by means of spring contacts fitted in the module, enabling stringent shock and vibration requirements such as those specified in the DIN EN 50155 railway standard to be met.

www.harting.com

CONGATEC PUTS AMD G-SERIES SOC 3W PROCESSOR ON QSEVEN

congatec is expanding its Qseven product range by adding the AMD Embedded G-Series SOC (System-on-Chip) platform. This single-chip solution combines the improved processing power of the "Jaguar" processor with the graphics core of AMD Radeon 8000 technology.

congatec currently offers three processors from the AMD Embedded G-Series SOC platform in the Qseven form-factor. The AMD GX-210HA 1.0GHz dual core (L2 cache 1MB) with 9W thermal design power (TDP) and the AMD GX-210JA 1.0GHz dual-core (L2 cache 1MB) with 6W TDP and an expected average power consumption of just 3W in a standard application will both be offered. For extreme environments, the module is also available in extended temperature range of -40°C to +85°C, featuring the AMD GX-209HA 1.0GHz dual-core (L2 cache 1MB). This AMD G-Series SOC is designed to require 33% less power than previously available AMD G-Series processors.

Users benefit from outstanding multimedia performance, excellent performance-per-watt ratios and flexible task distribution between CPU and GPU.

www.congatec.com